Braf-mutant Schwann cells divert to a repair phenotype to induce congenital demyelinating neuropathy

Elise Marechal[1], Patrice Quintana[1], Daniel Aldea[1], Grégoire Mondielli[1], Nathalie Bernard-Marissal[1], Mathias Moreno[1], Valérie Delague[1], Lauren A. Weiss[2,3], Anne Barlier[1,4], Heather C. Etchevers[1*]

[1] INSERM, MMG, U1251, MarMaRa Institute, Aix Marseille University, Marseille, France

[2] Department of Psychiatry and Behavioral Sciences, University of California, San Francisco, San Francisco, CA 94143, USA

[3] Institute for Human Genetics, University of California, San Francisco, San Francisco, CA 94143, USA

[4] AP-HM, MMG, MarMaRa Institute, La Conception Hospital Laboratory of Molecular Biology, Marseille, France.

Abstract

RASopathies are developmental disorders associated with mutations leading to constitutive activation of the Mitogen Activated Protein Kinase (MAPK) signaling pathway. Peripheral nerve enlargement and damage are recently reported symptoms in germline RASopathy patients. We characterized mouse models in which a frequent mutation of the MAPK effector Braf (V600E) in mosaic RASopathies is expressed in embryonic progenitors of Schwann cells. Postnatal mice develop an early, fully penetrant degenerative peripheral neuropathy. Symptoms appear before weaning, with sciatic nerve enlargement, loss of hindlimb muscle strength, and failure to thrive relative to littermates. The V600E catalytic domain mutation promotes expansion of a Jun+ Schwann cell repair state at the expense of mature, myelinating Schwann cells, preventing full peripheral myelination. Associated with the germline RASopathy cardio-facio-cutaneous syndrome, the *BRAF* (Q257R) mutation also prevents terminal differentiation of Schwann cells from patient-derived induced pluripotent stem cells. This study supports the likelihood that some of the genetic heterogeneity in human peripheral neuropathies may be imputed to somatic mosaicism in a contextually underexplored pathway. It also provides a mechanistic explanation for RASopathy-associated neuropathies.

Keywords: rare disease / mosaicism / signaling / neural crest / development

Abbreviations

- CHN: congenital hypomyelinating neuropathy
- DEG: differentially expressed genes
- FDR: false discovery rate
- g: grams
- *g*: standard gravity unit
- h: hours
- min: minutes
- Mpz/P0: Myelin protein zero
- PNS: peripheral nervous system
- SC: Schwann cell
- sec: seconds
- V600E: Missense substitution of valine by glutamate at position 600 of the BRAF protein sequence

Introduction

Oncogenic mutations in *BRAF* frequently drive human cancers, including malignant melanoma, thyroid, colorectal, lung, ovarian and breast cancers (Davies et al., 2002; Garnett and Marais, 2004; Xing et al., 2005). *BRAF* encodes a crucial serine/threonine protein kinase pivotal for transmitting external signals to the nucleus in the Mitogen-Activated Protein Kinase (MAPK) pathway. Its sustained activity is correlated with rapid cell cycling and resistance to apoptotic signals, contributing to tumorigenesis and cancer progression (Liu et al., 2007; Corazzari et al., 2015; Kawakami et al., 2016). However, mutations driving its constitutive activation are also the cause of a growing list of many rarer congenital diseases affecting other tissues, sometimes associated with cancer predispositions (Kratz et al., 2011).

RASopathies are a large class of developmental disorders arising from mutations in multiple genes encoding proteins of the MAPK pathway (Bentires-Alj et al., 2006; Rauen, 2013a). Activating mutations in *BRAF* have been identified in germline RASopathies such as cardio-facio-cutaneous syndrome (CFC; ORPHA:1340; Aymé et al., 2015) and Noonan syndrome with (ORPHA:500) or without (ORPHA:648) multiple lentigines. These and other RASopathies share overlapping clinical features, including reduced postnatal growth, dysmorphic facial features, melanocytic nevi or other pigmented lesions, congenital heart defects and tumor predispositions (Nava et al., 2007; Tartaglia et al., 2011). Germline RASopathies are multisystemic syndromes, but somatic RASopathies such as congenital melanocytic nevus (ORPHA:626), oculoectodermal (ORPHA:3339) or encephalocraniocutaneous lipomatosis (ORPHA:2396) syndromes can manifest in only one or many potential organ systems, depending on the extent of mosaicism (Maridet et al., 2016; Ramesh et al., 2017; Etchevers et al., 2018; Morren et al., 2024).

Peripheral nerve enlargement and damage have also been reported in patients with Noonan, CFC and related syndromes, and are among their lesser-known symptoms (Manci et al., 2005; De Ridder et al., 2022; Draaisma et al., 2023a). The structural integrity of the peripheral nervous system (PNS) is reliant on Schwann cells (SC), glial cells arising from neural crest cells and responsible for both myelination and peripheral nerve support (Le Douarin et al., 1991). Although neural crest cells are a transient migratory population in the embryo, after dissemination there persist Schwann cell precursors (SCP) from mid-gestation throughout life with more restricted stem cell characteristics. These are found in peripheral ganglia and along the paths of all postnatal sensory and autonomic nerves investigated to date (Adameyko et al., 2009; Balakrishnan et al., 2016; reviewed in Etchevers et al., 2019).

During PNS maturation, the axonal growth factor neuregulin-1 type III (Nrg1-III) binds to Erbb2 or Erbb4, receptor tyrosine kinases expressed on SCs to activate downstream signal transduction cascades involving the MAPK pathway (Meyer and Birchmeier, 1995; Riethmacher et al., 1997; Garratt et al., 2000; Nave and Salzer, 2006; Birchmeier and Nave, 2008; Newbern and Birchmeier, 2010). Multiple studies show that MAPK activation is required for the initiation and appropriate levels of myelination. Ablation of *Erk1* and *Erk2* at embryonic developmental stages significantly disrupts SC differentiation, leading to peripheral nerve hypomyelination (Newbern et al., 2011).

Mosaic expression of a constitutively active variant of *Mek1* (Mek1DD), the major kinase downstream from Braf activating Erk1 and Erk2, also induces neuropathy in mice but with hypermyelinated peripheral axons (Ishii et al., 2013; Sheean et al., 2014; Belin et al., 2019). Prolonged expression of the Mek1DD allele in SCs through *Cnp-Cre*-mediated recombination results in PNS myelin abnormalities, such as myelin infoldings/outfoldings and degenerated axons (Ishii et al., 2016). However, when a *Raf1* transgene is activated in adult myelinating SCs by induction at 4-6 weeks of age, it triggers the proliferation of progenitor-like SCs, resulting in less myelinated peripheral nerves, immune cell infiltration and severely impaired motor function within ten days (Napoli et al., 2012). Overexpression of *Raf1* or *Mek1* in SC *in vitro* also prevents their effective synthesis of myelin (Harrisingh et al., 2004; Ogata et al., 2004). Collectively, these studies suggest that the MAPK pathway is implicated in multiple processes to regulate PNS myelination, but the pathogenetic or compensatory mechanisms for neuropathies in the RASopathy spectrum have not yet been examined.

Here, we designed a mouse model to explore the effects of the constitutively activating *Braf*$^{V600E/+}$ mutation in progenitors of myelin-forming SCs in peripheral nerves. These mice develop an early and severe degenerative peripheral neuropathy with enlarged peripheral nerves. We demonstrate that *Braf*^{V600E} expression also promotes a repair phenotype in SC without exogenous nerve injury, characterized by expression of phosphorylated ERK1/2, immature SC-related genes, and induction of specific regulators such as Jun and Shh, but without effective remyelination over time. Complementing this *in vivo* model, we show that induced pluripotent stem cells (hiPSCs) from patients with CFC syndrome carrying a recurrent activating *BRAF* mutation (Q257R) are also unable to differentiate into myelin-competent SCs *in vitro*. Associated with significant axonal loss, sustained MAPK signaling throughout SC differentiation orients towards an inappropriate repair-like state rather than to myelination.

Materials and Methods

Generation of transgenic *P0-Cre*; *Braf*$^{V600E/+}$ or *Krox20-Cre*; *Braf*$^{V600E/+}$ mice and genotyping

All mice were maintained on outbred backgrounds to maximize genetic heterogeneity by crosses over multiple generations to CD1/Swiss mice purchased from Janvier Laboratories (France). *Lox-Stop-Lox-Braf*$^{V600E/+}$ (*LSL-Braf*$^{V600E/+}$) mice, carrying a T1799A mutation in a floxed construct containing an alternative exon 15 within the *Braf* locus (Mercer et al., 2005) (derived from RRID:IMSR_JAX:017928 but kindly provided by Prof. Richard Marais, University of Manchester, UK), were crossed to: (1) *P0(Mpz)-Cre* (derived from B6N.FVB-Tg(Mpz-cre)26Mes/J, RRID:IMSR_JAX:017927) (Feltri et al., 1999) or (2) Krox20-Cre (RRID:IMSR_JAX:025744) (Voiculescu et al., 2000) mice, to generate compound heterozygous *P0-Cre*$^{+/°}$; *Braf*$^{V600E/+}$ or *Krox20-Cre*$^{+/°}$; *Braf*$^{V600E/+}$ mice, called "mutant"; all other genotypes (WT$^{+/+}$, P0/Krox20-Cre$^{+/°}$ and *LSL-Braf*$^{V600E/+}$) were termed "control".

Genotyping of *LSL-Braf*$^{V600E/+}$ x *Cre* descendants was performed using PCR primers to detect the *LSL-Braf*$^{V600E/+}$ construction allele: *LSL-Braf-Forward:* (5′-GCCCAGGCTCTTTATGAGAA-3′) and *LSL-Braf-Reverse:* (5′-AGTCAATCATCCACAGAGACCT-3′) as well as generic *Cre* primers for both driver lines: *Cre-Forward*: (5'-TGATGGACATGTTCAGGGATC-3') and *Cre-Reverse*: (5'-CAGCCACCAGCTTGCATGA-3'). All PCR analyses were performed on DNA isolated from ear biopsies using Phire Tissue Master Mix PCR reagent (Thermo Fisher). The mice were kept in an animal facility with 12-hour light and 12-hour dark cycle and unrestricted access to other mice, water, and a regular diet. This animal study was reviewed and approved by the French accredited animal care and use committee (ACUC) C2EA-14 under the references 37-08102012 and 9522-2017040517496865v5.

Western Blot analyses

Mouse sciatic nerves were lysed in cold RIPA buffer (50 mM Tris (pH 8), 150 mM NaCl, 1% NP-40, 1% sodium deoxycholate, 0.1% sodium dodecyl sulfate (SDS) in the presence of 1X HALT protease inhibitor cocktail (1 mM AEBSF-HCl, 0.8 µM aprotinin, 50 µM bestatin, 15 µM E-64, 5 mM EDTA, 20 µM leupeptin, 10 µM pepstatin A; Thermo Fisher 78429). At 4°C, lysates were first sonicated for 3 cycles of 1 min pulse at 30 sec intervals in a Bioruptor (Diagenode) and then centrifuged at 4°C for 5 min at 1,000 *g*. Protein concentration was quantified by the DCProtein assay II (Bio-Rad 5000112) using an EnSpire Multimode plate reader (PerkinElmer) according to the manufacturer's protocol. Lysates were diluted in NuPAGE LDS Sample Buffer (Invitrogen, Thermo Fisher), heated 5 min at 100°C under reducing and denaturing conditions in the presence of 25 mM dithiothreitol, and 20 µg of protein was separated on 12% SDS-PAGE gels. Proteins were transferred onto a 0.45 µm

PVDF Immobilon-P membrane (Millipore, Merck) using the Pierce Power Blotter (Thermo Fisher). Membranes were blocked with 1X Tris-Buffered Saline-Tween (TBS-T; 50 mM Tris, 150 mM NaCl, 0.05% Tween-20, pH 7.6), containing 5% skim milk (1 hr at room temperature [RT]) and incubated with primary antibodies at 1:1000 dilution (overnight at 4°C): rabbit polyclonal anti-phospho (Thr202/Tyr204) Erk1/2 (#9101; Cell Signaling Technology), rabbit polyclonal anti-Erk1/2 (#9102; Cell Signaling Technology), rabbit monoclonal anti-Jun (60A8) (#9165; Cell Signaling Technology) or mouse monoclonal anti-GAPDH (#MAB374; Merck Millipore). After washes, cells were incubated in the blocking solution with the HRP linked anti-mouse or anti-rabbit secondary antibody (respectively #7076 or #7074; Cell Signaling Technology) at 1:10,000 dilution (1 hr at RT in the dark). Blots were developed with the Super Signal West Pico or Femto PLUS Chemiluminescent Substrate (Thermo Fisher). Chemiluminescent signals were detected using a CCD camera and Syngene software (G:BOX). PageRuler Prestained protein ladder (#26616; ThermoFisher Scientific) was used as a molecular weight marker. Total protein band intensity was measured using NIH Image J software v.1.54f (https://imagej.net/ij/) and normalized to the corresponding level of Gapdh to control for variations in loading. The measurement of phosphorylated proteins was reported relative to the overall expression level of the protein of interest.

Culture and differentiation of human pluripotent stem cells (hiPSC)

This study was conducted in accordance with the Declaration of Helsinki (The World Medical Association, 2022), the Belmont report (Office for Human Research Protections, 2018), and the French law on bioethics 2021-1017, promulgated on August 2, 2021 (*LOI n° 2021-1017 du 2 août 2021 relative à la bioéthique*, 2021), consistent with our institutional review board protocols.

Two cardio-facio-cutaneous (CFC) syndrome patients bearing a heterozygous germline *BRAF* Q257R mutation or their legal guardians provided written consent, as approved by the UCSF Human Research Protection Program (CHR #10-02794), to produce the human induced pluripotent stem cell (hiPSC) lines, RMK0056C and RMK0138C, as described (Yeh et al., 2018). The AG08H and hFF15 clones of healthy donor hiPSC lines were derived (CytoTune IPS 2.0 reprograming kit, Thermofisher) from commercial cell lines consented for research, AG08498 (RRID:CVCL_1Y51) and HFF-1 SCRC-1041 (RRID:CVCL_3285) respectively, as described (Dion et al., 2019). After the latter had been assessed for absence of Sendai virus or mycoplasma and maintenance of pluripotency by our institutional Cell Reprogramming and Differentiation Facility (MaSC) in Marseille, France, all lines were initially grown in mTeSR1 medium (Stemcell Technologies) on human embryonic stem cell-qualified Matrigel™ (354277; BD Biosciences) before long-term storage over liquid nitrogen.

Established hiPSC lines were thereafter thawed and cultured on six-well plates coated with Synthemax II-SC Substrate (#734-2634; Corning) at a working concentration of 0.025 mg/mL and maintained in an undifferentiated state using StemMACS iPS-Brew XF medium (#130-104-368; MACS Miltenyi Biotec). The hiPSC lines were incubated at 37°C and 5% CO_2 and media changed daily. When cells reached 60-80% confluence, they were passed using enzyme-free ReleSR (#05872; StemCell Technologies), adding 10 µM of ROCK inhibitor Y-27632 (#SCM75; Sigma-Aldrich) for the first 24 hours after passage.

For the directed differentiation of hiPSC into SC, we followed a published protocol (Hörner et al., 2021a). Differentiation of hiPSCs into SC was initiated when both control and mutant *BRAF* Q257R hiPSCs reached a confluence of 60%. Subsequently, cells were passaged every 6 days until day 31, at which point cells were passaged upon reaching 90% confluence, not necessarily synchronized between the cell lines. During the differentiation period, cell passaging was conducted as follows: at a 1:10 split on the 6th day, at a 1:6 split on the 12th and 18th days, and at a 1:4 split on the 24th day. From Day 31 onward, cell passaging was carried out at a 1:2 split to maintain an adequate cell density and prevent cellular death.

Total RNA isolation

Sciatic nerves from WT or *Braf*$^{V600E/+}$ animals of both sexes, and pellets of WT or *BRAF*$^{Q257R/+}$ hiPSC-derived SCP and immature Schwann cells (iSC) were stored at -80°C. Sciatic nerves on postnatal days 5 (P5) or 21 (P21) were lysed using ceramic beads in the FastPrep-24 homogenizer (MP Biomedicals) at 6 m/s for 50 sec and total RNA extracted with the RNeasy Lipid Tissue Mini Kit (#74804; Qiagen). For SCP (D18) and iSC (D31) differentiated from hiPSCs, total RNA was extracted using the NucleoSpin RNA Plus S kit (#740984; Macherey-Nagel). RNA concentrations were measured on a NanoDrop (NanoDrop TM 1000 Spectrophotometer; Thermo Fisher Scientific).

Library preparation and RNA-sequencing

RNA-sequencing and bioinformatics analysis was carried out at the GBiM Genomics and Bioinformatics facility from the U1251/Marseille Medical Genetics laboratory. We performed two different mRNA-sequencing analyses. The first was performed, on four replicates, on total RNA samples obtained from sciatic nerves at P5 and P21 collected from either WT or *Braf*$^{V600E+/-}$ mutant mice (16 samples in total). The second was performed on two or three replicates from hiPSC-derived SCP, iSC differentiated from two WT (hff15 and AG08H) or two *Braf*$^{Q257R/+}$ mutants (RMK0056C and RMK0138C) hiPSCs (29 samples in total). Following the RNA extraction, we evaluated the quality using the Agilent (Agilent Technologies). Only RNAs with RNA Integrity Numbers (RIN) exceeding 8 were considered

appropriate for sequencing. For each sample, a library was prepared from 1µg of total RNA for whole sciatic nerves or from 300ng of total RNA for differentiated cells, after capture of polyadenylated RNA using the KAPA mRNA HyperPrep kit (#KR1352-v7.21; Roche). The individual libraries were assessed using a Qubit™ and the Agilent Bioanalyzer dsDNA High Sensitivity Kit (Agilent Technologies). We sequenced at 2*76 base-pairs on a NovaSeq 6000 (Illumina) (from mouse sciatic nerves) or on at 2*101 base-pairs on a NovaSeq 6000 (Illumina) (from hiPSC-derived SC).

Data processing and differential gene expression analysis (DGE)

The quality of sequencing reads was assessed using fastQC (v0.11.5) (https://www.bioinformatics.babraham.ac.uk/projects/fastqc/). Raw sequencing reads were aligned on the GRCm39 mouse reference genome or on the GRCh38 human reference genome using STAR (v2.7.2b). Bam files were indexed and sorted using Samtools (v1.7). After mapping, the number of reads per feature (Ensembl or GENCODE v34 annotations for mouse or human data, respectively) was determined using StringTie v2.1.6.

Genes differentially expressed between conditions were identified using a Wald test in the DESeq2 package (v1.34.0). Differentially expressed transcripts with an adjusted P-value for FDR (False Discovery Rate) below 0.05 were considered significant (see Statistics, below). Relative expressions of the most variable features between samples were plotted as heatmaps using the Pheatmap R package. Differentially Expressed Genes (DEGs) were visualized in the form of volcano plots, representing the Log2FC (log2 of the expression -fold change) and the adjusted P-value, prepared using the EnhancedVolcano R package (Blighe et al., 2023).

Teased nerve fiber immunofluorescence

For immunochemistry on teased fibers, nerves were isolated from mice, fixed for 30 min (2 hr for mutants) in 4% paraformaldehyde in PBS at pH 7.4, washed in PBS and subsequently teased apart with insect pins onto Superfrost Plus glass slides. Slides were then dried overnight at RT and stored at -20°C. Teased sciatic nerves were permeabilized in acetone for 10 min at -20°C, washed in PBS, non-specific binding blocked for 1 hr at room temperature in PBS containing 5% w/v fish skin gelatin and 0.5% Triton-X100, then incubated with primary antibodies diluted in the blocking solution overnight at 4°C. After PBS rinses, slides were incubated with the appropriate Alexa Fluor-coupled secondary antibody (ThermoFisher) and DAPI (4',6-diamidino-2-phenylindole) diluted to 1/500 and 300 nM in the blocking solution for 1 hr at room temperature. Teased sciatic nerves were then washed and mounted in Prolong Diamond medium (#P36961; Invitrogen). Image stacks were acquired

using a super-resolution spinning disk confocal microscope (Nikon SoRa) and NIS-Elements software.

The following primary antibodies were used in this study: rat monoclonal to MBP at 1/250 (#MAB386; Sigma-Aldrich), rabbit polyclonal to Caspr at 1/50 (#ab34151; Abcam), rabbit polyclonal to Pmp2 at 1/100 (#12717-1-AP; ProteinTech), mouse monoclonal to Erbb3 at 1/100 (#MAB348; R&D Systems), rabbit polyclonal to S100b at 1/1000 (#HPA015768; Sigma-Aldrich), and mouse Shh at 1/100 (#5E1; DSHB). Alexa Fluor 488-coupled phalloidin was also used at a 1/500 dilution to label filamentous (F)-actin (ThermoFisher).

Electron microscopy (EM) and image analysis

Mouse sciatic nerve samples were dissected and fixed in fresh ice-cold 2% PFA + 2.5% glutaraldehyde in phosphate buffered saline at pH 7.4 for 7 hrs. After three washes in 0.1M sodium cacodylate buffer, nerves were post-fixed with 1% osmium tetroxide (OsO_4) for 2 hr on ice. The nerves were rinsed in distilled water and contrasted in aqueous 1% uranyl acetate solution overnight at 4°C. Samples were then dehydrated in a series of ethanol solutions of increasing concentrations for 20 min each and infiltrated with Epon resin in acetone (in ratios of 1:3, 2:2 and 3:1) for 2 hr each. Finally, nerves were embedded in fresh resin overnight and polymerized at 60°C for 48 hr. Semi-thin sections at 1 µm were stained with toluidine blue. Ultra-thin sections for EM were mounted on copper grids coated with Formvar membrane and contrasted with 2% uranyl acetate for 10 min and lead citrate for 5 min before imaging on an FEI Morgagni 120 kv electron microscope.

Analysis of sciatic nerve morphology

MyelTracer software (Kaiser et al., 2021) was used on 8-bit EM images to determine the *g*-ratio (axon diameter/fiber diameter), axon diameter, and the distribution of axons according to the thickness of the myelin sheath in control vs mutant sciatic nerves at P5 (n = 3 individuals per group) and at P28 (n = 2 individuals per group). The number of axons was counted using ImageJ software on lower magnification EM images of the sciatic nerve, comprising n = 3/3, n=5/4 and n=2/2 controls/mutants at P5, P21 and P28, respectively. Analyses were conducted without consideration of sex.

Enrichment analysis

Expression-dependent enrichment analysis was conducted using Gene Set Enrichment Analysis (GSEA) software v4.3.2 (Subramanian et al., 2005) with the mouse Wikipathway database to compute pathway enrichment scores in P0(Mpz)-*Braf*$^{V600E/+}$ (Mpz-*Braf*) sciatic nerves compared to controls. The same analysis was carried out using the human Reactome

database for *BRAF*$^{Q257R/+}$ hiPSC-derived SCP or iSC in comparison to control-differentiated hiPSCs.

Expression-independent enrichment analysis was performed using g:Profiler (Kolberg et al., 2023) or Enrichr-KG (Evangelista et al., 2023), interrogating the Wikipathway, KEGG, Reactome and Gene Ontology data sets.

Statistics

Statistical analyses were conducted using Prism v10.2.0 for Windows (GraphPad Software, Boston, Massachusetts USA, www.graphpad.com). Two-sided comparisons were assessed using unpaired Mann-Whitney or two-way ANOVA tests for non-parametric tests. For multiple comparisons, two-way ANOVA tests followed by Šidák's post-hoc method were used, or Student t-tests followed by Benjamini-Hochberg adjustment to control the False Discovery Rate (FDR) in DESeq2. Mendelian segregation was assessed with a chi-square contingency test. Data are presented as the mean ± standard error of the mean (s.e.m). $P > 0.05$ was considered as non-significant (ns), (*) $P < 0.05$; (**) $P < 0.01$; (***) $P < 0.001$; (****) $P < 0.0001$.

Results

Locomotor deficits and smaller body size in *Braf*$^{V600E/+}$ mice are associated with sustained sciatic nerve MAPK signaling

P0-Cre$^{+/°}$; *Braf*$^{V600E/+}$ mice, abbreviated hereafter as Mpz-*Braf* mice (Suppl Fig.1A), were born at the expected Mendelian ratios and remained asymptomatic for the first week. *Braf*$^{V600E/+}$ expression in neural crest-derived SC progenitors having expressed Mpz as early as embryonic day 12 (Hagedorn et al., 1999) does not affect embryonic or neonatal survival. However, from postnatal day (P)7, Mpz-*Braf* mutants developed signs of peripheral neuropathy including a trembling gait, abnormal postural reflexes of the hindlimbs and trailing legs (Fig. 1A). These phenotypes were fully penetrant. In addition, starting from P10, mutant mice consistently had a significantly reduced nose-to-tail length and proportionately reduced weight (Fig. 1B). Postnatal growth retardation was correlated with reduced transcription of *IGF1* in the liver of mutant mice (data not shown). Simultaneously, protein extracts from mutant sciatic nerves showed a significant increase in downstream Erk1/2 phosphorylation when compared to controls, both at early (P5, Fig. 1C) and late (P21, Fig. 1D) stages of SC-mediated myelination.

Braf$^{V600E/+}$ in SCs induces macroscopically enlarged peripheral nerves with widespread demyelination and axonal loss

Enlarged sciatic nerves in all Mpz-*Braf* mice were visible upon autopsies conducted at P5 and P21, where mutant nerves lacked the bands of Fontana (Fig. 2A). Mpz-*Braf* sciatic nerves grew significantly wider than in their wildtype littermates by P10 (0.48 ± 0.07 vs 0.31 ± 0.05 mm in controls), each reaching a stable diameter from P21 onwards (0.74 ± 0.09 vs 0.39 ± 0.05 in controls at P21, and 0.78 ± 0.05 vs 0.50 ± 0.04 mm in controls at P35, Fig. 2B). Similar enlargement was also evident in other peripheral nerves of Mpz-*Braf* mice at P21, including the peroneal, tibial, sural, and saphenous nerves (Supplementary Fig. 1B/C). In contrast to the mixed motor and sensory fibers in the sciatic nerve, the saphenous nerve is a purely sensory nerve that was nearly 2.6-fold wider in mutants (Supplementary Fig. 1D).

To evaluate the myelination dynamics in the Mpz-*Braf* sciatic nerve, we conducted ultrastructural electron microscopy (EM) analysis at P5, P21 and P28 (Fig. 2C and Fig. 3A). At P5, no discernible differences were observed in density (51,711 ± 2,235 axons/mm^2 in Mpz-*Braf* *vs* 47,895 ± 3,226 axons/mm^2 in controls), or axon diameter (1.447 ± 0.026 µm in Mpz-*Braf* *vs* 1.476 ± 0.072 µm in controls). This held true for all axon diameters (Fig. 2D and Supplementary Fig. 2 A/B). In addition, myelin thickness (as measured by the g-ratio, the ratio of the diameters of the outer fiber to the axon) remained unchanged in mutant nerves (Fig. 2E; 0.732 ± 0.019 in Mpz-*Braf* vs 0.708 ± 0.028 in controls; Supplementary Fig.2 C/D). The radial sorting and myelination processes therefore begin similarly in mutant and control peripheral nerves.

However, by P21, a significant decline in axon density was observed in Mpz-*Braf* mutants (4,060 ± 1,378 axons/mm^2 *vs* 36,172 ± 2,726 axons/mm^2 in age-matched controls, Fig. 2F). At P28, myelinated axons were even less dense in mutants (1,841 ± 465 axons/mm^2 *vs* 25,703 ± 2,812 axons/mm^2 in controls, Fig. 2G), and degenerating axons were visible (Fig. 3A). Extracellular collagen, fibroblasts and numerous SC nuclei were visible between remaining axons. The average diameter of these residual axons was significantly reduced (Fig. 3B; 1.89 ± 0.23 µm in Mpz-*Braf* vs 2.64 ± 0.07 µm in controls). Loss of axon density is primarily due to a decrease in large-caliber fibers of greater than 3 µm diameter (Fig. 3C and Supplementary Fig. 2E; on average: 8.7 ± 6.68% in Mpz-*Braf* vs 33.3 ± 5.59% in controls), suggesting their preferential degeneration. Myelinated axons display globally higher average g-ratios, indicating thinner myelin sheaths compared to those of age-matched control littermates (Supplementary Fig. 2F; average g-ratios: 0.66 ± 0.02 in Mpz-*Braf* vs 0.59 ± 0.0005 in controls).

We next analyzed 792 and 746 myelinated axons in mutant and control mice, respectively (Fig. 3D). Binning by width showed that small-caliber axons (<1 µm) exhibited a slightly significant increase in myelination (g-ratios of 0.47 ± 0.01 in mutants vs 0.52 ± 0.02 in controls, Fig. 3E). In contrast, medium- (1-3 µm diameter) and large-caliber axons (>3 µm) had significantly thinner myelin in mutants compared to controls (average g-ratios: 0.67 ± 0.03 vs 0.59 ± 0.005 for medium-caliber axons; and 0.75 ± 0.002 vs 0.60 ± 0.01 for large-caliber axons), confirming that the largest fibers were most severely affected in terms of myelination and persistence.

Striking myelin aberrations were visible in Mpz-*Braf* nerves after P21 (Fig. 4), including examples of tomaculae, infoldings, onion bulbs and degenerated axons, and focal hypermyelination of small-caliber axons, among other anomalies. These structures were interspersed with abundant extracellular collagen fibrils and tentacular fibroblasts (Fig. 4D). By P42, myelinated fibers were far sparser in transverse semi-thin sections of mutant than control sciatic nerves (Fig. 4E-F).

To extend these structural findings, we examined the distribution of key PNS proteins within Mpz-*Braf* nerves by isolating individual or small groups of sciatic nerve fibers before immunostaining at P5 and P21. Caspr immunofluorescence (Contactin-associated protein 1 or paranodin) showed that residual myelin internodes were irregularly spaced or absent along mutant axons (Fig. 5B,D,F,G). At P5, F-actin staining with fluorescently tagged phalloidin highlighted beads of myelin ovoids within teased mutant sciatic nerve fibers, indicating the early breakdown process of myelin even during its establishment in neighboring axons (Fig. 5B-D). Unlike their control littermates, by P21 (Fig. 5E), Mpz-*Braf* mice displayed demyelinated regions, devoid of myelin basic protein (Mbp) along individual fibers (Fig. 5F). Furthermore, the abundance of DAPI-labelled nuclei along fibers between nodes highlights elevated retention of immature Mpz-*Braf* SCs (Fig. 5F).

Braf$^{V600E/+}$ sciatic nerves display early altered expression of myelin sheath genes *in vivo*

To identify transcriptional changes associated with congenital demyelination after MAPK pathway activation, we conducted bulk RNA-sequencing on microdissected Mpz-*Braf* and control sciatic nerves derived from four distinct mice at both P5 and P21 (Fig. 6, Supplemental Table 1). At P5, we identified 2,540 differentially expressed genes (DEGs) between mutant and control nerves (padj< 0.05). Among these, 1,407 genes were over-expressed, and 1,133 genes were under-expressed. At P21 with the same thresholds, 10,409 DEGs were identified, comprising 5,398 over-expressed and 5,011 under-expressed

genes (Fig. 6A). The observed demyelination and axonal degeneration phenotype in Mpz-*Braf* sciatic nerves is therefore associated with large-scale changes in gene transcription.

The myelin sheath predominantly consists of lipids (70% to 85%) and myelin-related proteins (15 to 30%) (Poitelon et al., 2020). By P21, Gene Set Enrichment Analysis (GSEA) using the Wikipathway database highlights significant downregulation of pathways related to cholesterol regulation in *Braf*-mutant sciatic nerves (Fig. 6B). “Cholesterol biosynthesis” and “cholesterol metabolism” ranked as the top affected pathways, with 15 out of 15 (100%) and 37 out of 49 (75.5%) downregulated genes associated with these respective terms (Fig. 6C). Among the most downregulated genes at P21 was *Hmgcr* (11.4-fold), encoding a rate-limiting enzyme in cholesterol biosynthesis (Ohashi et al., 2003), and *Fa2h* (7.9-fold), encoding fatty acid 2-hydroxylase and critical for synthesis of myelin 2-hydroxy-glycosphingolipids (Maldonado et al., 2008) (Supplemental Table 1). Paradoxically, *Pmp2* and *Omg* mRNA levels were significantly upregulated in P5 Mpz-*Braf* sciatic nerves but not significantly different from control littermates at P21 (Fig. 6D).

Although the transcription of major myelin components such as *Mpz* (myelin protein zero), *Mbp* (myelin basic protein) and *Pmp22* (peripheral myelin protein 22*)* were not yet significantly altered at P5, several less abundant myelin sheath transcripts had already begun to be under-expressed, such as those for periaxin (*Prx*), myelin-associated oligodendrocyte basic protein (*Mobp*), plasmolipin (*Pllp*) and myelin-associated glycoprotein (*Mag;* Figure 6D, Supplemental Table 1). Alterations in cholesterol regulation were not yet seen in P5 *Braf*-mutant sciatic SC, but a member of the fatty acid-binding protein family, *Pmp2* (encoding a fatty acid binding protein, also called *Fabp8*) and *Omg* (oligodendrocyte myelin glycoprotein) displayed 4.4-fold and 9.7-fold increases, respectively. By P21, when myelination is usually well advanced in young mouse sciatic nerves, we observed a downregulation of transcripts encoding both major *Mpz* (7,9-fold), *Mbp* (11,6-fold), *Pmp22* (7,3-fold) and other peripheral myelin proteins (Fig. 6D). Transcriptional disruption of myelin synthesis is thus a cell-autonomous response to sustained Braf and Erk1/2 signaling in SCPs after birth.

Alteration in the transcriptional control of myelination in *Braf*-mutant sciatic nerves

In light of the significant decrease in multiple myelin-associated genes in the Mpz-*Braf* model, we analyzed the expression of transcription factors (TF) known to positively or negatively control the process of myelination. The major transcriptional activators *Egr2* (early growth factor response 2, also named Krox20; Topilko et al., 1994) and *Sox10* (SRY-box TF 10; Peirano et al., 2000), remained unaffected at P5. However, by P21, when myelination is

usually well advanced in young mouse sciatic nerves, mutant SCs underwent a modest but significant downregulation of *Egr2* TF expression (1.4-fold) (Fig. 7A). We identified globally similar transcription of genes in the Mpz-*Braf* model as compared to a model of hypomyelinating neuropathy triggered by a hypomorphic *Egr2* allele (*Egr2*$^{lo/lo}$; Le et al., 2005), with 99/110 genes (90%) or 98/107 genes (91.5%) commonly up or downregulated, respectively (Fig. 7B). Sciatic nerve hypomyelination observed in the Mpz-*Braf* model is correlated with decreased *Egr2*-driven transcription.

Simultaneously, many other known SC-associated transcriptional repressors of myelination (Jessen and Mirsky, 2008) were significantly upregulated in mutant sciatic nerves at P21, including *Jun* (2-fold), *Egr1* (3-fold), *Egr3* (2.8-fold), *Zeb2* (2-fold), and *Sox2* (6-fold), the last of which had already been overexpressed at P5 (1.4-fold) (Fig. 7A). The increase in *Jun* mRNA at P21 translated into 4.5 times more protein (also known as c-jun) in mutant than control nerves (Fig. 7C).

To see if the PNS effects of oncogenic Braf could be reproduced by restricting it to *Egr2*-expressing cells *in vivo* and to compare with the *Mek1DD* model (Sheean et al., 2014), we crossed heterozygous LSL-*Braf*$^{V600E/+}$ mice to mice carrying one copy of the Cre recombinase under the control of the *Egr2* promoter (*Egr2*-Cre or *Krox20*-Cre), expressed in SCs from mid-gestation onwards (Topilko et al., 1994; Supplementary Fig 1A). Surprisingly, mutant neonates were never obtained from this breeding, a significant departure from the expected yield, which demonstrates fully penetrant embryonic lethality of compound heterozygotes (Fig. 7D).

The *Pmp2* and *Omg* genes are overexpressed in sciatic nerves with hypermyelinating neuropathies induced by either *Egr2*-driven *Mek1* (*Mek1DD*) in SCs (Sheean et al., 2014), or by *Thy1*-driven, proteolytically processed type III neuregulin-1 in axons (Velanac et al., 2012; Belin et al., 2019). *Thy1* encodes a cell surface glycoprotein widely expressed on neural and hematopoietic precursors. Both models drive constitutive activation of the MAPK pathway in Egr2-expressing SC and are postnatally viable. Since *Mek1* functions downstream of *Braf*, we compared the available transcriptomic data from hypermyelinating *Egr2*-Cre; *Mek1DD* mutant sciatic nerves at P8 and P30 with Mpz-*Braf* sciatic transcriptomes at P5 and P21 (Fig. 7E). There was a robust positive correlation at both early and late stages of myelination (Spearman's correlation coefficients of r = 0.8153 and r = 0.7325, respectively). In parallel, we conducted the same comparative analysis with transcriptomic data from a concurrent model of hypomyelinating neuropathy, resulting from SC-specific depletion (*Egr2*-Cre) of the upstream MAPK pathway phosphatase Shp2, encoded by *Ptpn11*, a model for NS (Sheean et al., 2014). We observed negative correlation of DGE at the earlier stage (P5 vs P8, r = -

0.4674) and poor correlation after weaning (P21 vs P30, r = 0.3048; Fig. 7F). The Mpz-*Braf* phenotype is thus distinct from these previously explored models of MAPK gain-of-function in the PNS.

Ectopic expression of repair-specific genes in uninjured *Braf*$^{V600E/+}$ sciatic nerves

Transcripts significantly overexpressed at P5 and sustained through P21 in mutant sciatic nerves may reflect potentially direct effects of MAPK signaling on Mpz-*Braf* SC. We classified the 175 genes in common that were significantly upregulated by two-fold or more at both stages with annotations from Wikipathways, KEGG and REACTOME (Supplementary Fig 3A). There was significant enrichment of the terms “spinal cord injury”, “G1 to S cell cycle control” and “glycosaminoglycan biosynthesis”. GSEA analysis showed further enrichment of the “spinal cord injury” term at P21 (Supplementary Fig 3B). We then compared the overall transcriptomes of Mpz-*Braf* sciatic nerves at P5 or P21 with those of a 6- to 8-week mouse model of axotomy at seven days post-injury (Arthur-Farraj et al., 2017a). Positive correlations were present at both stages, improving over time (Fig. 7G and Supplementary Fig 3C,D; Spearman’s correlation coefficients of r = 0.4816 and r = 0.7683, respectively) and demonstrating thereby that the transcriptomic signature of juvenile Mpz-*Braf* sciatic nerves correlates with acquisition of multiple molecular hallmarks of the response to nerve injury.

Following physical injury such as crush or axotomy, SCs undergo extensive reprogramming, ensuring the re-expression of immature genes and transcription of repair-associated genes. These genes are found at low levels or are absent at both immature or earlier stages of SC lineage and can serve as markers to distinguish repair SCs in injured adult nerves from immature SCs (Hashimoto et al., 2008; Piirsoo et al., 2010; Lin et al., 2015). A well-known example is the transcription factor Jun, significantly transcribed and translated at P21 (Fig. 7A,C). Several secreted ligands reported to depend on Jun and specific to the repair phenotype were, as expected, strongly upregulated in Mpz-*Braf* sciatic nerves as early as P5 (Fig. 7H). Among these were *Shh* (Sonic hedgehog; 73.5-fold at P5 and 140.6-fold at P21) and the neurotrophic factor *Gdnf* (Glial cell line-derived neurotrophic factor; 4.8-fold at P5, 32.8-fold at P21). However, at P5, *Jun* transcription was not yet significantly changed in mutants (Fig. 7A), suggesting that its increase in mutant nerves correlates with, rather than is the principal effector of, *Shh* and *Gdnf* upregulation.

We next examined the colocalization in teased nerve fibers of S100B (Fig. 6A), an intermediate filament common to SCP and their SC and melanocyte derivatives, and Shh. Shh is a specific growth factor important for neural crest differentiation and postnatally transcribed in repair SCs upon nerve injury (Hashimoto et al., 2008). Both among the top

genes upregulated at P5, Shh and S100B proteins were localized to the same cells in P21 Mpz-*Braf* mutant sciatic nerves, when compared to control nerves processed in parallel both before and after image acquisition**.** Transcription of glial NRG1-I (Neuregulin-1 type I), another growth factor secreted by SCs after nerve injury (Stassart et al., 2013) and in various chronic demyelinating diseases (Fledrich et al., 2019), was significantly upregulated at both stages: 54.5-fold at P5 and 126-fold at P21. Its ErbB3 receptor, also increased after nerve damage (Carroll et al., 1997), was indeed induced in mutant nerves at P21 (2.6-fold more transcript) (Fig. 7H). More Erbb3 protein immunofluorescence was also observed in mutant than control nerves, be it in the presence of degenerating, Pmp2-containing myelin or not (Fig.8B-F). Concomitant downregulation of *Sema5a* transcription, a consequence of nerve injury in rat SC (Brosius Lutz et al., 2022), is also consistent with the induction of the "injured nerve" activated state in sciatic glia (Supplementary Table 1). Despite the heightened expression of these markers of the repair program in Mpz-*Braf* sciatic nerves, the pronounced and progressive axonal degeneration with impaired locomotion show that compensation for demyelination was ineffective *in vivo*.

Impaired Schwann cell differentiation of CFC patient-derived hiPSCs

To assess the effects on SC of the heterozygous activating *BRAF*Q257R mutation found in CFC patients, we differentiated hiPSC cell lines derived from two unrelated patients (RMK0056C and RMK0138C, Yeh et al., 2018) into SC *in vitro* (Hörner et al., 2021a) and compared their maturation status with that of two control hiPSC lines (HFF15, AG08H). Cells of the control lines were morphologically similar to each other throughout the directed differentiation protocol, but one of the mutant cell lines (RMK0138C) displayed a distinct shape and density. It required more frequent passages to maintain similar density and failed to develop the elongated shape and long projections characteristic of SCPs in the three other lines, even after 90 days of differentiation *in vitro* (Fig. 9A).

All four hiPSC-derived SC lines were subjected to bulk RNA-sequencing on two key days (D) of the protocol: on D18, at a committed SCP-like stage, and on D31, for a stage more analogous to late SCP or immature SC (Fig. 9A). We analyzed the mutant lines both together and separately for differentially expressed genes relative to the control lines (Supplemental Table 2). Pathway analyses of the 380 DEGs common to both mutant cell lines at D31 (Fig. 9B) using the human REACTOME database showed downregulation of genes associated with keratinocytes and basal epidermal wound response, including eight keratin genes (REAC:R-HSA-6809371, Supplemental Table 2, Fig. 9C). Another significantly enriched pathway was "EGR2 and SOX10-mediated initiation of SC myelination" (REAC:R-HSA-9619665, Fig. 9C,D). Among the downregulated transcripts therein were *EGR2, MBP*,

PRX (encoding Periaxin) and *LAMA2* (encoding the alpha-2 chain of laminin-211, a major component of SC basal lamina).

In contrast, *POU3F2*, encoding a transcription factor also called BRN2 or OCT7, was commonly upregulated in both CFC patient-derived cell lines (on average 5.2-fold and 3.6-fold at D18 and D31, respectively; Supplemental Table 2). In mice, *Pou3f1* and *Pou3f2* are transiently expressed in the early SC lineage, peaking in the first week after birth, with some functional redundancy (Jaegle et al., 2003). Since they are also important effectors of neurogenesis, able singly or in combination to induce multipotent cells to become neurons both *in vivo* (Dominguez et al., 2013) and *in vitro* (Zhu et al., 2014), we re-examined the cell type annotations associated with genes upregulated over time in concert with *POU3F2* human SC differentiated from each CFC line when compared to both control hiPSC together. When annotated by Enrichr-KG (Evangelista et al., 2023) with databases related to human disease (Grissa et al., 2022), quantitative proteomics of the Cancer Cell Line Encyclopedia (Nusinow et al., 2020) and a single-cell atlas of human gene expression during development (Cao et al., 2020), annotations associated with the multipotency of neural crest-derived SCPs were significantly enriched. Top terms included “melanoma” and the proteome of an amelanotic, *V600E*-mutated melanoma cell line A2058; proteomes of a *P53*-mutated lung neuroendocrine carcinoma (NCI-H446) and a *NRAS*^{Q61L}-mutated neuroblastoma (SK-N-AS) cell lines, and lung or heart (“visceral” or parasympathetic) autonomic neurons (Fig. 9E). These findings suggest that maintenance of MAPK signaling after birth in immature SC of both mice and humans also maintains their capacity to co-express gene regulatory modules and transcriptional programs typical of their natural alternatives in terms of lineage differentiation (Adameyko et al., 2009; Furlan et al., 2017), which are normally restricted.

Discussion

Clinical signs overlap broadly between RASopathies because they are caused by mutations of highly pleiotropic components of the MAPK signal transduction pathway. Combinations of the most penetrant phenotypes can indicate a specific diagnosis. Major indications that a patient may carry a pathogenic *BRAF* mutation include a combination of degrees of facial dysmorphy, congenital heart defects and rhythm anomalies, deficient somatic growth due at least in part to frequent feeding difficulties, dysfunctional ectodermal appendages and pigmentation anomalies of the skin, cognitive impairments to varying degrees, ocular symptoms such as strabismus, hypotonia, epilepsy, and cryptorchidism (undescended testicles) in boys (Champion et al., 2011; Rauen, 2013b, 2007). Cardio-facio-cutanous or Noonan syndromes are first suspected on the basis of such clinical grounds but are now

formally diagnosed as such after molecular confirmation in concert with the clinical signs (Rauen, 2013b, 2007).

Lesser-known symptoms of patients with congenital RASopathy syndromes include peripheral neuropathy (Draaisma et al., 2023b; Vizcaino et al., 2020), short stature (Andreadi et al., 2012; Feng et al., 2023; Gripp et al., 2007; Kang and Lee, 2019) and dysplastic bone lesions (Dong et al., 2022) as well as increased tendency to benign or malignant tumorigenesis (Bowen et al., 2011; Brems et al., 2012; Gripp et al., 2007). Musculoskeletal symptoms and lipomas are also commonly associated with mosaic forms of RASopathies (Hafner and Groesser, 2013) as are epidermal (Morren et al., 2024) or melanocytic naevi (Dessars et al., 2009), sometimes in combination (Carli et al., 2022). Mutations in the *RASA1* gene, encoding the Ras suppressor p120 RasGAP, are responsible for a specific multifocal capillary and arteriovenous malformation syndrome (Eerola et al., 2003) but also cause vein of Galen malformations (Zhao et al., 2023). However, similar bone and vascular malformations are also common hallmarks of mosaic PIK3CA-related overgrowth syndromes, in which PI3K signaling rather than MAPK signaling is sustained (Kurek et al., 2012; Lindhurst et al., 2012; Mirzaa et al., 2016). These even occur in combination in patients with mosaic RASopathies such as giant melanocytic nevi with BRAF p.V600E mutations (Al-Olabi et al., 2018; Etchevers et al., 2018).

In order to tease apart the mechanisms through which activation of PI3K and/or MAPK signaling during prenatal development lead to convergent congenital malformations in specific organ systems, it is important to develop conditional models in which effects of changes in these pathways can be experimentally isolated and thereby studied (Gualtieri et al., 2021; Marechal et al., 2022). The phenotype of the mouse model presented here, expressing a constitutively active form of Braf in only those cells having once transcribed the *Mpz* gene, casts new light on pathophysiological mechanisms in some peripheral neuropathies as well as on the short stature and failure to thrive reported in people affected by RASopathy syndromes.

The postnatal growth phenotype

Small body size in germline RASopathies is unlikely to be only caused by feeding anomalies, but also to endocrine disruption (Siano et al., 2022). The conditional Mpz-*Braf* mouse, with its pre-weaning growth retardation, complements a series of RASopathy animal models that display failure to thrive in the early postnatal period after germline mutations in *Kras* (Hernández-Porras et al., 2014), *Braf* (Urosevic et al., 2011; Andreadi et al., 2012; Inoue et al., 2014; Moriya et al., 2015), *Raf1* (Wu et al., 2011), *Ptpn11* (Araki et al., 2004) or *Sos1* (Chen et al., 2010), all activating the MAPK pathway. Short stature is most commonly

reported in NS patients carrying *PTPN11* hypermorph mutations such as D61G, and can be phenocopied in *Ptpn11*$^{D61G/+}$ "NS" mice accompanied by GH resistance, with normal or elevated GH levels (Araki et al., 2004; Serra-Nédélec et al., 2012). Only half of the heterozygous NS mice are born and no homozygotes, due to severe heart malformations (Araki et al., 2004) but by P15, growth retardation is accompanied in surviviors by a decrease of 40% in serum Igf1 levels. NS mice show constitutive phosphorylation of Erk1/2 downstream of Igf1r and Ghr with or without GH stimulation, leading to feedback inhibition of Igf1 synthesis, while inhibition of activated Mek1 can partially restore Igf1 production and body length (Serra-Nédélec et al., 2012).

CFC syndrome patients bearing either *BRAF* or *MEK1* mutations, as well as Costello syndrome (CS) patients with *HRAS* mutations, may also suffer from growth hormone (GH) deficiency (Gripp et al., 2007). In a series of 26 Korean patients with CFC or NS-like syndromes with germline *BRAF* mutations, 20 were significantly (more than -2SD) short for their age and some were GH-sensitive. Another *BRAF*-mutated CFC patient treated for precocious puberty not only had GH-responsive growth retardation but also hyperprolactinemia with no pituitary tumor (Çelik et al., 2014). On one hand, in the light of the fully penetrant association of neuropathy and small size in Mpz-*Braf* mice, MAPK pathway inhibitors may improve statural outcomes and thereby, quality of life in young GH-resistant CFC patients. On the other hand, our observations in conjunction with these and other case reports (Siano et al., 2022) indicate that a minority population derived from Mpz-expressing cells could play an unsuspected paracrine role in postnatal pituitary function of RASopathy patients.

A peripheral neuropathy results from constitutively activated Braf in Schwann cells

The trembling and locomotor troubles we observed in Mpz-*Braf* mice affected the hindlimbs without extending to other body areas before 6 weeks. However, purely sensory nerves, such as the saphenous, and other mixed nerves, such as the sural or trigeminal nerves, were visibly enlarged on autopsy. These observations in the absence of signs of suffering make the Mpz-*Braf* mouse a tractable model in which to carry out further behavioral or electrophysiological studies of RASopathy-associated neuropathy. Our findings furthermore pinpoint the Schwann cell as a candidate initiator of the neuromuscular outcomes.

Unlike for some trauma- or toxin-induced nerve injuries, nerves affected by peripheral neuropathies do not regenerate. Highly heterogeneous on both a genetic and phenotypic level, peripheral neuropathies can be divided into major functional classes depending on the types of axons affected (sensory, motor, autonomic or mixed). Small sensory fibers, thinly myelinated or unmyelinated, enable the perception of pain, temperature, stretch and other

sensations. The neuronal soma of such fibers are located in peripheral ganglia, where all neurons, satellite glia and Schwann cells derive from embryonic neural crest cells and persistent Schwann cell precursors (reviewed in Etchevers et al., 2019). Small-fiber neuropathy typically involves the loss of these small-caliber axons and can engender pain (nociceptive) and/or autonomic nervous system (sudomotor, adrenergic, enteric) dysfunctions (Themistocleous et al., 2014). Such neuropathies develop for example with diabetes mellitus, alcohol use disorder, auto-immunity or chemotherapy. As yet, there have been few reports of neuropathic pain in RASopathy patients. Nonetheless, in a small cohort of four children with a confirmed germline RASopathy and hypertrophic spinal nerves, and in a separate young adult CFC patient since his childhood, neuropathic pain was present in all and muscle weakness in three of the five (DeRoos et al., 2007; Draaisma et al., 2023b). Mpz-*Braf* mice appear to proportionally gain, rather than lose, small-caliber axons in the sciatic nerve.

Four other NS children have also been recently reported with early-onset myasthenia (Pugliese et al., 2024). Neuropathic pain was not reported nor nerve size assessed by imaging, but evidence for functional neuromuscular junction (NMJ) defects led the investigators to treat with drugs enhancing NMJ transmission (cholinesterase inhibitor for one and a β2-adrenergic agonist for the other). Two patients responded well to this therapy (Pugliese et al., 2024). At all ages, 162 patients with CFC, NS, CS, and neurofibromatosis type 1 (NF1) RASopathies, and a distinct cohort of 21 NF1 patients, also showed significant deficits in handgrip strength (Souza et al., 2009; Stevenson et al., 2012). An early motor or mixed sensory-motor deficit of varying degrees of severity is thus present in many RASopathy patients. In the Mpz-*Braf* mouse, motor impairments were observed in a mosaic setting, where only Schwann cell progenitors expressed the constitutively active form of Braf. This implies that muscular weakness and atrophy in *BRAF*-mutated CFC patients (DeRoos et al., 2007) may be result from an indirect effect of peripheral neuropathy and NMJ aberrations.

Neuromuscular implications of mosaic MAPK activation

In support of this conjecture, hiPSC-derived SC positively influence acetylcholine receptor density on myotubes in three-way co-cultures with motoneurons (Hörner et al., 2021b). Nonetheless, a primary deficit in myofiber differentiation has also been observed in mice bearing a CFC-like p.L597V germline *Braf* mutation (Maeda et al., 2021). Quadricep biopsies from two NS patients showed a ten-fold increase in innervated yet ectopic muscle spindle fibers, the stretch proprioceptors of striated muscle encapsulated by connective tissue at the muscle belly. The capsules were thickened and fibrotic (de Boode et al., 1996).

During normal muscle regeneration after toxin-induced muscle damage, periostin, an extracellular matrix (ECM) protein of the NMJ and muscle spindle encoded by the *Postn* gene, is increased, where it plays a non-cell-autonomous role to prevent muscle fiber loss during the regenerative process (Ito et al., 2021). However, in a distinct genetic mouse model of muscular dystrophy, periostin was pathologically upregulated. This was correlated with extensive fibrosis and enhanced muscle wasting that was partially rescued on a *Postn*-null background (Lorts et al., 2012). Mpz-*Braf* sciatic nerves show a remarkable 7.4-fold overexpression of *Postn* at P21 compared to controls and over time compared to P5 mutants. In contrast, in control nerves it is usually downregulated by 5.5-fold over the same interval. *In vitro*, *POSTN* is 5-fold less transcribed in SC induced from patient hiPSC compared to control cells (Supplementary Tables). These observations are compatible with a scenario where Schwann cells in response to MAPK signaling can regulate endoneurial fibroblasts to augment periostin and ECM production. Helpful after traumatic injury to contain damage, sustained MAPK activity in SC of RASopathy patients may induce fibrosis both in the nerve and at the NMJ.

Residual axons in the sciatic nerves of Mpz-*Braf* mutant mice were smaller and more abundant as a population than in control nerves, with less degeneration and paradoxically thicker myelin sheaths. Large axons were preferentially lost by P28 (equivalent to mouse adolescence). Motoneurons of the spinal cord supply the large axons in the sciatic nerve. Speed of conduction, ensured by Schwann cell myelination of these motor axons, enables rapid skeletal muscle response. Mpz-*Braf* mice remain mobile and can climb on or enter their paper shelters despite progressive hindlimb motor impairment through the first two postnatal weeks, which remains stable thereafter until P42. Their hindlimbs are most clearly affected. Demyelination of motor axons in peripheral neuropathies can lead to permanent motoneuron loss as well as secondary axon degeneration. These symptoms are observed in the second most common form of Charcot-Marie-Tooth disease, CMT1B, which is caused by *MPZ* mutations (reviewed in Moss et al., 2021). The Mpz-*Braf* mouse appears to undergo a congenital demyelinating, as opposed to a dysmyelinating, neuropathy. Most fibers at P5 appear to have normal myelin structure in electron microscopy, despite already being visibly if not significantly enlarged (Figure 2A-B). However, confocal microscopy of the actin cytoskeleton and immunofluorescence showed that ovoids of degenerating myelin and diffuse spreading of paranodal proteins like Caspr along axons could already be observed at P5 (Figure 5B-D). This indicates that individual fiber demyelination is indeed congenital but only overtakes collective physiological myelination after the second week.

Fibrotic effects of RASopathy-induced neuropathy

The striated bands of Fontana normally visible in peripheral nerves are due to light reflected from aligned axons coursing in their normal sinusoidal path and are altered in models of demyelinating peripheral neuropathy (Alvey et al. 2018). Normally, sensory and motor axons are longer than the peripheral nerves in which they course in order to adapt to stretch induced by animal movement. A large nerve has more axons than a small nerve. A striking aspect of the Mpz-*Braf* phenotype was the early and persistent loss of the bands of Fontana in mutant animals from all nerves examined, in conjunction with increased nerve width. Electron microscopy showed that although there were many nuclei of fibroblasts and Schwann cells in mutant nerves, the residual fibers were instead surrounded by abundant fibroblast projections and collagen filaments. Without massive infiltration of immune cells, there were significantly fewer axons overall in the widened sciatic nerve, translating into reduced axonal density.

This fibrotic phenotype is correlated with strong upregulation of transcription of the multifunctional hyaluronan receptor CD44 *in vivo*. *Cd44* was already significantly upregulated relative to controls in Mpz-*Braf* sciatic nerves at P5 and by over ten-fold in P21 mutant nerves, whereas it is usually downregulated by more than two-fold over the same time period. However, the enriched human iSC from patients showed less than half the transcription in control cells of *CD44*. Given that blockage of CD44 with a monoclonal antibody can prevent the formation of an excessively fibrotic spinal cord scar after injury (Guo et al., 2024), CD44 may be a biomarker for excessive ECM synthesis at the expense of axon maintenance in peripheral neuropathy. Furthermore, pleiotrophin, a secreted heparin-binding growth factor produced by human SC within *NF1*-mutant neurofibromas (Tian et al., 2024) and shown to directly stimulate fibrosis, is also significantly overexpressed in Mpz-*Braf* sciatic nerves at P21. Topical application of a MAPK inhibitor to cutaneous SC prevents such fibrosis in a preclinical model for NF1 (Coulpier et al., 2023), raising the exciting possibility that such an approach could be used to treat RASopathy-associated neuropathy.

Constitutively active Braf induces an abnormally sustained Schwann cell repair state

MAPK pathway signaling is upregulated in Schwann cells in response to peripheral nerve injury such as crush or axotomy (Sheu et al., 2000; Harrisingh et al., 2004; Agthong et al., 2006, 2009). A complex set of interactions between glia, axons, and mesenchymal cells such as immune cells, fibroblasts and vascular pericytes establishes a novel environment that may be, but is not always, permissive to nerve regeneration. After existing myelin is cleared away, mature SC remaining at the as-yet denervated site begin to express the requisite master transcription factor Jun and downstream proteins only synthesized by repair-competent SC,

while repressing myelin synthesis genes (Arthur-Farraj et al., 2012). This repair signature includes transcription of genes for growth factors like Gdnf, Artn, Shh and Ptn; intracellular effectors like Rgs8 and Igfbp3; additional transcription factors like Sox2 and Foxd3; membrane-bound adhesion molecules and receptors like Ncam1, Mcam, Cd44 and Alk; and the ECM proteins Postn and Tnc (Arthur-Farraj et al., 2017b, 2012). All of these were significantly and abundantly upregulated in mosaic Mpz-*Braf* sciatic nerves. In contrast, only ALK and SOX2 were differentially upregulated at either stage assessed in the differentiation protocol for SC from CFC patient versus control hiPSC lines. While the physiological SC repair cell is a transient state, sustained Sox2 expression by SC blocks their ability to myelinate peripheral nerves and maintains them in a proliferative, non-differentiated state (Le et al., 2005b; Roberts et al., 2017). *SOX2* is expressed by undifferentiated primary human neural crest cells both *in vitro* and *in vivo* (Thomas et al., 2008). Our findings identify Sox2 as another intrinsic regulator of myelinating SC *in vivo* and that its expression correlates with maintenance of an immature, proliferative state in concert with the repair program in Mpz-*Braf* peripheral nerves.

However, the upregulation of Jun and acquisition of the full repair phenotype in sciatic nerves is likely to be contingent on conditions we did not provide *in vitro.* Potential intermediaries include tissue-resident or infiltrating immune cells, endoneurial fibroblasts or vascular pericytes. We have observed that endoneurial fibroblasts and vascular pericytes, in addition to myelinating Schwann cells (Warner et al., 1998) strongly express the Egr2 transcription factor (Marechal et al., 2022). These derive from a specialized multipotent SC progenitor originating in the embryonic neural crest, known as the boundary cap cell (Maro et al., 2004). Boundary cap cells express Egr2 from E12.5 at the junctions between the dorsal and ventral roots and the spinal cord and migrate along developing peripheral nerves to the skin among other sites, guiding vascular development in parallel (Gerschenfeld et al., 2023; Gresset et al., 2015). EGR2 directly regulates myelination in both humans and animal models; both dominant and recessive mutations can cause congenital hypomyelinating forms of human Charcot-Marie-Tooth (CMT) neuropathy (Bellone et al., 1999; Timmerman et al., 1999; Warner et al., 1999, 1998)(Bellone et al., 1999; Timmerman et al., 1999; Warner et al., 1999, 1998). Given the importance of this transcription factor to multiple cell types (McCowan et al., 2021), it is not surprising that *Krox20Cre;Braf*(V600E/+) mice were embryonic lethal. A tamoxifen-inducible construct would permit better control and study of the effects of somatic mosaicism at relevant time points or body locations.

Normal and pathophysiological dynamics in myelination: two sides of the same coin

The Mpz-*Braf* mouse models peripheral demyelination and large axonal loss in the presence of a congenitally overactive *Braf*$^{V600E/+}$ mutation and shows that this phenotype is

accompanied by the presence of repair-type, immature Jun-expressing SC in the absence of nerve injury. Perinatal demyelination occurs simultaneously with the normal period of myelination, as evidenced at P5 by the presence of myelin ovoids that indicate early Wallerian degeneration. Constitutive activation of Mek1 *(MEK1DD)* during early embryonic stages results instead in a neuropathic hypermyelination (Ishii et al., 2013; Sheean et al., 2014; Ishii et al., 2016; Belin et al., 2019) while nonetheless showing global transcriptomic similarity of affected sciatic nerves with our model.

Although activation of constitutively active Mek1 by targeted induction in adult SC has no documented detrimental effect, it prevents lesional repair or functional recovery thereafter. Such mice are unable to regenerate experimentally injured peripheral nerves, which instead undergo rapid Wallerian degeneration (Cervellini et al., 2018). In contrast, the expression during adulthood of a reversibly inducible form of constitutively active Raf1 (also known as Craf) in *Mpz*-positive, myelinating SC is already sufficient to provoke a severe hypomyelinating neuropathy accompanied by SC dedifferentiation (Harrisingh et al., 2004; Napoli et al., 2012). Similar to the Mpz-*Braf* model, these SC both proliferate and secrete factors capable of recruiting inflammatory cells in the absence of nerve injury (Napoli et al., 2012). When the induction was stopped, nerves remyelinated and functional recovery took place.

The overexpression of Raf family kinases thus appears to induce dedifferentiation and early demyelination at any point in the SC lifetime, while the embryonic overexpression of downstream Mek1 leads to excessive myelin deposition (also functionally detrimental) and postnatal induction does not result in an immediate, spontaneous phenotype. It may be that with longer follow-up, such mice develop schwannomas or other tumors. The Mpz-*Braf* phenotype is complementary to previously explored models of MAPK gain-of-function in the PNS and may allow the study of how other signaling pathways impact the dynamics of demyelination and remyelination.

Our work also raises the possibility that using targeted deep-sequencing gene panels developed for suspicion of RASopathy could help screen for somatic mutations of MAPK pathway members in DNA derived from the tissue biopsy taken for clinical diagnosis of CMT patients, when no other disease-causing variant is identified. In summary, these results underscore the critical role of the timing and context of mutational induction, as well as the importance of finely regulated expression of the MAPK pathway, in myelination and nerve repair.

Data availability

Raw and processed RNA-sequencing data from this study have been deposited to the Gene Expression Omnibus (GEO) and assigned the accession identifiers GSE262047 and GSE262048.

The full electron microscopy imaging dataset has been deposited at the BioImage Archive (BIA) with the accession S-BIADxxxxx .

Websites

Rare disease ORPHA codes are maintained at https://www.orpha.net and available on https://www.orphadata.com/ (Aymé et al., 2015).

fastQC (v0.11.5) is available at https://www.bioinformatics.babraham.ac.uk/projects/fastqc/ and EnhancedVolcano at https://bioconductor.org/packages/EnhancedVolcano.

Fiji/ImageJ open software is available from https://imagej.net/ij/

Figure Legends

Figure 1: Constitutive MAPK activation mediated by the BrafV600E/+ mutation in Schwann cells induces early peripheral neuropathy in mice.

(A) At P21, Mpz-*Braf* mice displayed abnormal hind limb postural reflexes and dragging legs when walking on the wire cage (indicated by arrows), indicating a functional defect in peripheral nerves. (B) Body weight was monitored at various time points after birth (P5, P10, P21, P35 and P42) in both Mpz-*Braf* and control mice (n = 28 *vs* 8 at P5, n = 15 *vs* 5 at P10, n = 54 *vs* 45 at P21, n = 14 *vs* 10 at P35, n = 5 *vs* 5 at P42, in control *vs* mutant nerves, respectively). Western Blot analysis of total and phosphorylated Erk1/2 signaling performed on sciatic nerves lysates from (C) P5 and (D) P21 control and Mpz-*Braf* mice. Gapdh was used as loading control. Protein levels were estimated by densitometric analysis using ImageJ software, with n=4 *vs* 5 in control/mutant at P5 and n=13 *vs* 15 control *vs* mutant sciatic nerves at P21. Statistical significance was assessed by either (B) two-way ANOVA followed by Šidák's post-hoc test, or by (C/D) unpaired Mann-Whitney test. (ns) not significant; (*) $P < 0.05$; (**) $P < 0.01$; (***) $P < 0.001$; (****) $P < 0.0001$.

Figure 2: Myelination initiation is not impaired in *Braf*-mutant sciatic nerves, while maintenance is compromised.

(A) Macroscopic examination of control and mutant sciatic nerve at P5 and P21. Arrows indicate Fontana bands, present only in control nerves. (B) Sciatic nerve diameter measurements at P5, P10, P21, and P35 in both Mpz-*Braf* and control mice (n = 11 *vs* 6 at P5, n = 6 *vs* 4 at P10, n = 15 *vs* 10 at P21, and n = 5 *vs* 5 at P35; in control *vs* mutant

nerves, respectively). (C) Representative electron micrographs images of sciatic nerve cross-sections at P5 and P21 from control and mutant mice. (D) Mean axon diameter per genotype was quantified at P5 (n = 3 in each group). (E) Scatter-graph demonstrating g-ratios (ratio of outer fiber diameter to axon diameter) to assess myelin thickness as a function of axon diameter at P5. The g-ratio analysis was performed using MyelTracer, with a total of n = 803 *vs* 811 myelinated axons for the control *vs* mutant nerves, from 3 individuals in each group (significance tests for correlations are indicated by asterisks). (F) Quantitative analysis of the number of axons per mm^2 in sciatic nerves from control or Mpz-Braf mice at P21 (control, n = 5; mutant, n = 4). (G) Quantitative analysis of the number of axons per mm^2 in the sciatic nerves from controls or Mpz-Braf mice at P28 (n=2 in each group). Statistical tests were performed using two-way ANOVA followed by Šidák's post-hoc test. (ns) not significant; (*) P < 0.05; (**) P < 0.01; (***) P < 0.001; (****) P < 0.0001.

Figure 3: The *Braf*$^{V600E/+}$ mutation in Schwann cells early triggers degeneration of large-caliber axons alongside demyelination.

(A) Representative electron micrographs images of sciatic nerve cross-sections at P28 from control and mutant mice. (B) Mean axon diameter per genotype was quantified at P28 (n = 2 in each group). (C) Assessment of the genotype-dependent distribution of myelinated axon diameters (in µm) in mutant or control sciatic nerves at P28, represented as percentages. (D) Scatter-graph demonstrating g-ratios (ratio of outer fiber diameter to axon diameter) to assess myelin thickness as a function of axon diameter (0-1 µm: small "a", 1-3 µm: medium "b", and >3 µm: large "c") at P28. The g-ratio analysis was performed using the MyelTracer software, with a total of n = 792 *vs* 746 myelinated axons were analyzed for control *vs* mutant nerves, from 2 individuals in each group (significance tests for correlations are indicated by asterisks). (E) Comparison of g-ratio distributions across distinct axonal populations stratified by diameter ranges (small "a", medium "b", and large "c"). Statistical tests were performed using two-way ANOVA followed by Šidák's post-hoc test. (ns) not significant; (*) P < 0.05; (**) P < 0.01; (***) P < 0.001.

Figure 4: Abnormal axonal and myelin structures in Mpz-*Braf* mice.

(A-D) Representative electron micrographs images of sciatic nerve cross-sections from control or mutant mice at P21 (left panel; A/C) and P28 (right panel; B/D). In control sciatic nerves (A/B), typical compact myelin and Remak bundles (RB) are observed. However, *Braf*-mutant nerves (C/D) exhibit both myelin and axon abnormalities, including focal hypermyelination or thickened myelin around axons with significantly reduced diameter (*), SC myelinating multiple axons of medium caliber (**), infoldings (***), various stages of myelin decompaction and axonal degeneration (arrows). Fb, fibroblast. Dashed boxed areas denote extracellular collagen bundles. Scale bars = 5 µm, 2 µm or 1 µm as indicated. (E-F)

Semi-thin sections at P42, obtained from both Mpz-*Braf* and control mice, with loss of myelinated axons, occasional figures of hypermyelination and overall reduced axonal density in the mutant sciatic nerve. Scale bar = 50 µm.

Figure 5: Myelin disassembly and segmental demyelination in teased sciatic nerves from Mpz-*Braf* mice.

Teased fibers from sciatic nerves of control (A, E) and Mpz-*Braf* mice (B-D, F-G) at P5 (top panels) and P21 (bottom panels) were immunostained with antibodies against Mbp and Caspr and Alexa Fluor 488-conjugated phalloidin, demonstrating the presence of myelin ovoids (white arrowheads), fewer apparent nodes of Ranvier with dispersed paranodal Caspr staining (orange arrowheads), and segmental demyelination of Mpz-*Braf* teased sciatic nerves. DNA was labeled by DAPI (grey). Maximum intensity z-projection images were generated in B, E and F with Nikon NIS-Elements Viewer software. Scale bars: 50 µm (A/B/F) or 10 µm (C/E/G).

Figure 6: Comparative transcriptomic analysis reveals downregulation of myelin sheath components in *Braf*-mutant sciatic nerves.

(A) RNA-seq analysis was performed in control and Mpz-*Braf* mutant sciatic nerves (n = 4 per genotype). Volcano plots depict the DEGs in *Braf*-mutant sciatic nerves relative to controls at P5 (left panel) and P21 (right panel). An adjusted p-value < 0.5 and Log2FC <-1 (blue) or >1 (red) were used as thresholds to define DEGs. The top 15 DEGs are labeled on each graph according to Manhattan distance. (B) Volcano plots illustrate the differentially enriched pathways provided by GSEA through the WEB toolkit Web Gestalt (Liao et al., 2019) using mouse Wikipathway database. Significantly enriched pathways are defined using a false discovery rate (FDR) < 0.05 and normalized enrichment score (NES) < -1 (blue) or >1 (red). The size diameter of circle is proportional to gene ratio (count of core enrichment genes / count of pathway genes). (C) Enrichment plot for cholesterol biosynthesis using Wikipathway database, corresponding to the most significant gene set downregulated in mutant sciatic nerves (p-value and FDR < 0.001, NES = -2.3). (D) Dot plot displaying the Log2 fold change (Log2FC) of myelin-related genes (with *Mpz*, *Pmp22*, and *Mbp* in bold, representing the primary genes composing the myelin sheath). A slash denotes genes that are not differentially transcribed.

Figure 7: Decrease in expression of *Egr2* and its target genes in Mpz-*Braf* nerves, accompanied by an increase in expression of negative regulators of myelination including *Jun* and *Sox2.*

(A) Dot plot displaying the Log2 fold change (Log2FC) of transcription factors acting as positive (Sox10, Egr2) or negative regulators (Jun, Sox2, and the other genes) of myelination

in mutant versus control sciatic nerves at P5 and P21, derived from bulk RNA-sequencing data. Crossed-out boxes denote genes that are not significantly dysregulated. (B) Enrichment plot for upregulated (up panel) or downregulated genes (bottom panel) in a mouse model carrying a hypomorphic allele of *Egr2* (Le et al., 2005a) highlighted that a large majority of genes are commonly deregulated between this model and the *Mpz-Braf* model at P21. (C) Western Blot analysis of JUN expression in sciatic nerve lysates from P21-aged Mpz-*Braf* and control mice. GAPDH was detected as a loading control. Relative protein abundance was quantified by densitometry using ImageJ software, with n=13 control and n=13 mutant sciatic nerves. Statistical significance was assessed by an unpaired Mann-Whitney test, (****) $P < 0.0001$. (D) The distribution of genotypes at birth resulting from the mating of heterozygous LSL-*Braf*$^{V600E/+}$ mice with *Egr2-Cre* mice was significantly different from expected ($P<0.0001$, chi-square 24.21, df 3), demonstrating fully penetrant prenatal lethality. (E-F) Spearman's correlation was calculated on bulk RNA-sequencing data generated from Mpz-*Braf* sciatic nerves at P5 (top panel) or P21 (bottom panel), and DEG data sets obtained from mouse models with SC-specific (E) overexpression of a constitutively active form of Mek1 (*Egr2-Cre*; *Mek1*DD) or (F) knock-out of *Shp2* (*Egr2-Cre*; *Shp2*$^{f/f}$) at P8 and P30. (G) Spearman's correlation between bulk RNA-sequencing data generated from the Mpz-*Braf* model at P21 and DEG data 7 days after peripheral nerve injury in mice (Arthur-Farraj et al., 2017a). (H) Log2-fold changes (Log2FC) of known repair-associated genes obtained from bulk RNA-sequencing of Mpz-*Braf* sciatic nerves at P5 and P21 as compared to control nerves of the same stage.

Figure 8: Activation of injury-related genes in *Braf*V600E/+ sciatic nerves.

Teased fibers from sciatic nerves of P21 control and Mpz-Braf mice were stained with Alexa Fluor 488-conjugated phalloidin in combination with immunostaining for (A) S100B and Shh, or (B-E) Pmp2 and Erbb3. DNA was labeled with DAPI (grey). Maximum intensity z-projection images were generated with Nikon NIS-Elements Viewer software. Scale bars: 50 µm (B) or 10 µm (A/F).

Figure 9: Patient-derived immature Schwann cells co-express signatures of epidermal cells types and autonomic neurons during *in vitro* differentiation

(A) Schematic representation of the differentiation of human induced pluripotent stem cells (hiPSCs) into SC, derived from two WT (AG08H, HFF15) or two CFC patients carrying the *BRAF* p.Q257R mutation (RMK0056C, RMK0138C). D0: hiPSCs; D6: multipotent neural crest-like cells (NCCs); D12: presumably committed NCC; D24: SC precursors (SCP); D31: immature SC (iSCs); D90: myelin-competent SC. Representative bright-field images of cells during the differentiation protocol are shown at D13, D19, a day after passage on D32 and at

D95-100, after five days' exposure to ascorbic acid. Scale bar = 100 µm for all frames. (B) Euler diagram showing the number of common/specific dysregulated genes (p-value < 0.05, Log2FC > 1 or < -1) in RMK0056C and RMK0138C mutant cells compared to control cells (HFF15) at D21 of differentiation. (C) Bubble plot of the enrichment analysis performed on the common 380 dysregulated genes in RMK0056C and RMK0138C. Gene set names from the REACTOME database are indicated on the y-axis. Gene sets are ranked according to significance level (-log adjusted p-value). The size of the dots represents the number of queried genes present in the corresponding pathway, and the color corresponds to the gene ratio (number of queried genes present in the gene set / gene set size). (D) Enrichment plot for Egr2 and Sox10 mediated initiation of SC myelination using Reactome database, corresponding to the significant gene set downregulated in RMK0056C and RMK0138C cell lines after 30 days of differentiation. (E) Enrichr-KG analysis of the most significantly enriched terms across three additional databases (Descartes Cell Types and Tissue 2021, Jensen DISEASES and CCLE Proteomics 2020) highlight the close lineage relationship between Schwann cell progenitors and either melanocytes ("melanoma" and "skin cancer", the A2058 cell line) or neuroendocrine cells ("visceral neurons in lung/heart", the SKNAS and NCIH446 cell lines).

Supplementary Figure 1: Peripheral nerve morphology in mutant and control mice reveals enlarged nerves.

(A) Generation of *Mpz-Cre*; *Braf* $^{V600E/+}$ or *Krox20-Cre*; *Braf* $^{V600E/+}$ knock-in mice was achieved by crossing heterozygous LSL-*Braf* $^{V600E/+}$ mice with mice carrying the Cre recombinase under the control of the P0/*Mpz* promoter or the *Egr2*/Krox20 promotor, expressed in SCs from a progenitor state. (B-C) Exposed dissection of sciatic, peroneal, sural, tibial, and saphenous peripheral nerves in control and Mpz-*Braf* mice at P21. (D) Saphenous nerve diameter was significantly greater at P21 in Mpz-*Braf* (mean, 0.31 ± 0.02 mm) than in control mice (mean, 0.12 ± 0.01 mm; n=6 animals per group). Statistical significance was assessed by an unpaired Mann-Whitney test (**) P < 0.01.

Supplementary Figure 2: The diameters of myelinated axons in *Braf*-mutant sciatic nerves are abnormally reduced, with a loss of large-caliber axons.

(A) Quantitative analysis of the number of axons per mm^2 in the sciatic nerves of Mpz-*Braf* mice at P5 (n=3 per group). (B) Assessment of the genotype-dependent distribution of myelinated axon diameters (in µm) in mutant or control sciatic nerves at P5, represented as percentages. (C-F) Mean g-ratio per genotype was quantified at (C) P5 (n=3 per group) or (F) P28 (n=2 per group). (D) Comparison of g-ratio distributions (myelin thickness) across distinct axonal populations stratified by diameter ranges in µm (<1.5, 1.5-2, >2) at P5. (E) Comparison of axon diameter distribution at P28 in µm (small <1, medium 1-3 and large >3)

in control and Mpz-*Braf* mutant sciatic nerves, represented as percentages (n=2 in each group). Statistical tests were performed using two-way ANOVA followed by Šidák's post-hoc test. (ns) not significant; (*) $P < 0.05$.

Supplementary Figure 3: The transcriptome of Mpz-*Braf* sciatic nerves of mice correlates with that of recovery from nerve injury.

(A) Top: Euler diagram showing the number of upregulated genes (p-value < 0.05, Log2FC > 1) in Mpz-*Braf* mice sciatic nerves at P5 and P21 compared to their corresponding controls. Bottom: Bubble plot of the enrichment analysis performed on the common 175 upregulated genes at P5 and P21. Gene set names are indicated on the y-axis with their corresponding dataset ('WP': Wikipathways; 'REACT': REACTOME; KEGG). Gene sets are ranked according to their significance level (-Log adjusted p-value). The size of the dots represents the number of queried genes present in the corresponding pathway, and the color corresponds to the gene ratio (number of queried genes present in the gene set / gene set size). (B) Gene set enrichment analysis (GSEA) plots performed using the "WP spinal cord injury gene set", highlighting a highly significant enrichment score in the Mpz-*Braf* model at P5 and P21. (C) Spearman's correlation between bulk RNA-sequencing data generated from the Mpz-*Braf* model at P5 and DEG data after peripheral nerve injury in mice (Arthur-Farraj et al., 2017a). (D) Enrichr-KG analysis of the most significantly enriched terms across two additional databases (Tabula Muris and WikiPathway_2021_Human) highlight the relationship of commonly upregulated genes with the significant enrichment of terms associated with ectoderm-derived stem cells ("Stem Cell of Epidermis Skin" and "Neuronal Stem Cell Brain Non-Microglia" sharing many genes) and appendage differentiation ("Hair Follicle Development: Organogenesis) as well as the re-entry into cell division ("Cell Cycle", "G1 to S cell cycle control") and translation ("Cytoplasmic Ribosomal Proteins") necessary to assume a glial repair phenotype, of which many genes are associated with the term "Spinal Cord Injury".

Acknowledgements

The authors declare that they have no conflict of interest. This work was made possible by the Association Française contre les Myopathies (AFM-Téléthon) grant MoThARD to VD and HCE, the National Institutes of Health New Innovator award (1DP2OD007449) to LAW, and Horizon Europe HORIZON-MISS-2021-CANCER-02-03 MELCAYA (101096667) to HCE. EM was supported by the AFM-Téléthon, the Asociación Española de Nevus Gigante Congénito (AsoNevus, Spain), Naevus 2000 France-Europe (France) and the Marseille Rare Diseases Institute (MarMaRa) of Aix-Marseille University. We are grateful to C. Humbert, C. Castro, N. Trévisiol and C. Aubert of the MMG Genomics and Bioinformatics facility (GBiM) for assistance with RNAseq and analyses; Dr. N. Broucqsault, Dr. F. Magdinier, O. Hadadeh and C. El Yazidi of the Marseille Stem Cell (MaSC) core facility for control hiPSC cell lines and initial quality control; Dr. T.-T. Mac and Dr. T. Fauquier for their advice on hiPSC maintenance; and the PiCSL-France BioImaging core facility, supported by ANR-10-INBS-04, and Dr. C. Leterrier and Dr. L. Fourel of the Institute of NeuroPhysiopathology, CNRS-Aix Marseille University, for their assistance with microscopy.

References

Adameyko, I., Lallemend, F., Aquino, J.B., Pereira, J.A., Topilko, P., Müller, T., Fritz, N., Beljajeva, A., Mochii, M., Liste, I., Usoskin, D., Suter, U., Birchmeier, C., Ernfors, P., 2009. Schwann cell precursors from nerve innervation are a cellular origin of melanocytes in skin. Cell 139, 366–379. https://doi.org/10.1016/j.cell.2009.07.049

Agthong, S., Kaewsema, A., Tanomsridejchai, N., Chentanez, V., 2006. Activation of MAPK ERK in peripheral nerve after injury. BMC Neurosci. 7, 45. https://doi.org/10.1186/1471-2202-7-45

Agthong, S., Koonam, J., Kaewsema, A., Chentanez, V., 2009. Inhibition of MAPK ERK impairs axonal regeneration without an effect on neuronal loss after nerve injury. Neurol. Res. 31, 1068–1074. https://doi.org/10.1179/174313209X380883

Al-Olabi, L., Polubothu, S., Dowsett, K., Andrews, K.A., Stadnik, P., Joseph, A.P., Knox, R., Pittman, A., Clark, G., Baird, W., Bulstrode, N., Glover, M., Gordon, K., Hargrave, D., Huson, S.M., Jacques, T.S., James, G., Kondolf, H., Kangesu, L., Keppler-Noreuil, K.M., Khan, A., Lindhurst, M.J., Lipson, M., Mansour, S., O'Hara, J., Mahon, C., Mosica, A., Moss, C., Murthy, A., Ong, J., Parker, V.E., Rivière, J.-B., Sapp, J.C., Sebire, N.J., Shah, R., Sivakumar, B., Thomas, A., Virasami, A., Waelchli, R., Zeng, Z., Biesecker, L.G., Barnacle, A., Topf, M., Semple, R.K., Patton, E.E., Kinsler, V.A., 2018. Mosaic RAS/MAPK variants cause sporadic vascular malformations which respond to targeted therapy. J. Clin. Invest. 128, 1496–1508. https://doi.org/10.1172/JCI98589

Andreadi, C., Cheung, L.-K., Giblett, S., Patel, B., Jin, H., Mercer, K., Kamata, T., Lee, P., Williams, A., McMahon, M., Marais, R., Pritchard, C., 2012. The intermediate-activity L597VBRAF mutant acts as an epistatic modifier of oncogenic RAS by enhancing signaling through the RAF/MEK/ERK pathway. Genes Dev. 26, 1945–1958. https://doi.org/10.1101/gad.193458.112

Araki, T., Mohi, M.G., Ismat, F.A., Bronson, R.T., Williams, I.R., Kutok, J.L., Yang, W., Pao, L.I., Gilliland, D.G., Epstein, J.A., Neel, B.G., 2004. Mouse model of Noonan syndrome reveals cell type- and gene dosage-dependent effects of Ptpn11 mutation. Nat. Med. 10, 849–857. https://doi.org/10.1038/nm1084

Arthur-Farraj, P.J., Latouche, M., Wilton, D.K., Quintes, S., Chabrol, E., Banerjee, A., Woodhoo, A., Jenkins, B., Rahman, M., Turmaine, M., Wicher, G.K., Mitter, R., Greensmith, L., Behrens, A., Raivich, G., Mirsky, R., Jessen, K.R., 2012. c-Jun Reprograms Schwann Cells of Injured Nerves to Generate a Repair Cell Essential for Regeneration. Neuron 75, 633–647. https://doi.org/10.1016/j.neuron.2012.06.021

Arthur-Farraj, P.J., Morgan, C.C., Adamowicz, M., Gomez-Sanchez, J.A., Fazal, S.V., Beucher, A., Razzaghi, B., Mirsky, R., Jessen, K.R., Aitman, T.J., 2017a. Changes in the Coding and Non-coding Transcriptome and DNA Methylome that Define the Schwann Cell Repair Phenotype after Nerve Injury. Cell Rep. 20, 2719–2734. https://doi.org/10.1016/j.celrep.2017.08.064

Arthur-Farraj, P.J., Morgan, C.C., Adamowicz, M., Gomez-Sanchez, J.A., Fazal, S.V., Beucher, A., Razzaghi, B., Mirsky, R., Jessen, K.R., Aitman, T.J., 2017b. Changes in the Coding and Non-coding Transcriptome and DNA Methylome that Define the Schwann Cell Repair Phenotype after Nerve Injury. Cell Rep. 20, 2719–2734. https://doi.org/10.1016/j.celrep.2017.08.064

Aymé, S., Bellet, B., Rath, A., 2015. Rare diseases in ICD11: making rare diseases visible in health information systems through appropriate coding. Orphanet J. Rare Dis. 10, 35. https://doi.org/10.1186/s13023-015-0251-8

Balakrishnan, A., Stykel, M.G., Touahri, Y., Stratton, J.A., Biernaskie, J., Schuurmans, C., 2016. Temporal Analysis of Gene Expression in the Murine Schwann Cell Lineage and the Acutely Injured Postnatal Nerve. PLOS ONE 11, e0153256. https://doi.org/10.1371/journal.pone.0153256

Belin, S., Ornaghi, F., Shackleford, G., Wang, J., Scapin, C., Lopez-Anido, C., Silvestri, N., Robertson, N., Williamson, C., Ishii, A., Taveggia, C., Svaren, J., Bansal, R., Schwab,

M.H., Nave, K., Fratta, P., D'Antonio, M., Poitelon, Y., Feltri, M.L., Wrabetz, L., 2019. Neuregulin 1 type III improves peripheral nerve myelination in a mouse model of congenital hypomyelinating neuropathy. Hum. Mol. Genet. 28, 1260–1273. https://doi.org/10.1093/hmg/ddy420

Bellone, E., Di Maria, E., Soriani, S., Varese, A., Doria, L.L., Ajmar, F., Mandich, P., 1999. A novel mutation (D305V) in the early growth response 2 gene is associated with severe Charcot-Marie-Tooth type 1 disease. Hum. Mutat. 14, 353–354. https://doi.org/10.1002/(SICI)1098-1004(199910)14:4<353::AID-HUMU17>3.0.CO;2-4

Bentires-Alj, M., Kontaridis, M.I., Neel, B.G., 2006. Stops along the RAS pathway in human genetic disease. Nat. Med. 12, 283–285. https://doi.org/10.1038/nm0306-283

Birchmeier, C., Nave, K.-A., 2008. Neuregulin-1, a key axonal signal that drives Schwann cell growth and differentiation. Glia 56, 1491–1497. https://doi.org/10.1002/glia.20753

Blighe, K., Rana, S., Lewis, M., 2023. Blighe K, Rana S, Lewis M (2023). EnhancedVolcano: Publication-ready volcano plots with enhanced coloring and labeling. R package version 1.20.0.

Bowen, M.E., Boyden, E.D., Holm, I.A., Campos-Xavier, B., Bonafé, L., Superti-Furga, A., Ikegawa, S., Cormier-Daire, V., Bovée, J.V., Pansuriya, T.C., Sousa, S.B. de, Savarirayan, R., Andreucci, E., Vikkula, M., Garavelli, L., Pottinger, C., Ogino, T., Sakai, A., Regazzoni, B.M., Wuyts, W., Sangiorgi, L., Pedrini, E., Zhu, M., Kozakewich, H.P., Kasser, J.R., Seidman, J.G., Kurek, K.C., Warman, M.L., 2011. Loss-of-Function Mutations in PTPN11 Cause Metachondromatosis, but Not Ollier Disease or Maffucci Syndrome. PLOS Genet. 7, e1002050. https://doi.org/10.1371/journal.pgen.1002050

Brems, H., Pasmant, E., Van Minkelen, R., Wimmer, K., Upadhyaya, M., Legius, E., Messiaen, L., 2012. Review and update of SPRED1 mutations causing legius syndrome. Hum. Mutat. 33, 1538–1546. https://doi.org/10.1002/humu.22152

Brosius Lutz, A., Lucas, T.A., Carson, G.A., Caneda, C., Zhou, L., Barres, B.A., Buckwalter, M.S., Sloan, S.A., 2022. An RNA-sequencing transcriptome of the rodent Schwann cell response to peripheral nerve injury. J. Neuroinflammation 19, 105. https://doi.org/10.1186/s12974-022-02462-6

Cao, J., O'Day, D.R., Pliner, H.A., Kingsley, P.D., Deng, M., Daza, R.M., Zager, M.A., Aldinger, K.A., Blecher-Gonen, R., Zhang, F., Spielmann, M., Palis, J., Doherty, D., Steemers, F.J., Glass, I.A., Trapnell, C., Shendure, J., 2020. A human cell atlas of fetal gene expression. Science 370, eaba7721. https://doi.org/10.1126/science.aba7721

Carli, D., Cardaropoli, S., Tessaris, D., Coppo, P., La Selva, R., Cesario, C., Lepri, F.R., Pullano, V., Palumbo, M., Ramenghi, U., Brusco, A., Medico, E., De Sanctis, L., Ferrero, G.B., Mussa, A., 2022. Successful treatment with MEK-inhibitor in a patient with NRAS-related cutaneous skeletal hypophosphatemia syndrome. Genes. Chromosomes Cancer 61, 740–746. https://doi.org/10.1002/gcc.23092

Carroll, S.L., Miller, M.L., Frohnert, P.W., Kim, S.S., Corbett, J.A., 1997. Expression of neuregulins and their putative receptors, ErbB2 and ErbB3, is induced during Wallerian degeneration. J. Neurosci. Off. J. Soc. Neurosci. 17, 1642–1659. https://doi.org/10.1523/JNEUROSCI.17-05-01642.1997

Çelik, N., Cinaz, P., Bideci, A., Yüce, Ö., Emeksiz, H.C., Döğer, E., Çamurdan, O., 2014. Cardio-Facio-Cutaneous Syndrome with Precocious Puberty, Growth Hormone Deficiency and Hyperprolactinemia. J. Clin. Res. Pediatr. Endocrinol. 6, 55–58. https://doi.org/10.4274/Jcrpe.1151

Cervellini, I., Galino, J., Zhu, N., Allen, S., Birchmeier, C., Bennett, D.L., 2018. Sustained MAPK/ERK Activation in Adult Schwann Cells Impairs Nerve Repair. J. Neurosci. Off. J. Soc. Neurosci. 38, 679–690. https://doi.org/10.1523/JNEUROSCI.2255-17.2017

Champion, K.J., Bunag, C., Estep, A.L., Jones, J.R., Bolt, C.H., Rogers, R.C., Rauen, K., Everman, D., 2011. Germline mutation in BRAF codon 600 is compatible with human

development: De novo p.V600G mutation identified in a patient with CFC syndrome. Clin. Genet. 79, 468–474. https://doi.org/10.1111/j.1399-0004.2010.01495.x

Chen, P.-C., Wakimoto, H., Conner, D., Araki, T., Yuan, T., Roberts, A., Seidman, C.E., Bronson, R., Neel, B.G., Seidman, J.G., Kucherlapati, R., 2010. Activation of multiple signaling pathways causes developmental defects in mice with a Noonan syndrome–associated Sos1 mutation. J. Clin. Invest. 120, 4353–4365. https://doi.org/10.1172/JCI43910

Corazzari, M., Rapino, F., Ciccosanti, F., Giglio, P., Antonioli, M., Conti, B., Fimia, G.M., Lovat, P.E., Piacentini, M., 2015. Oncogenic BRAF induces chronic ER stress condition resulting in increased basal autophagy and apoptotic resistance of cutaneous melanoma. Cell Death Differ. 22, 946–958. https://doi.org/10.1038/cdd.2014.183

Coulpier, F., Pulh, P., Oubrou, L., Naudet, J., Fertitta, L., Gregoire, J.-M., Bocquet, A., Schmitt, A.-M., Wolkenstein, P., Radomska, K.J., Topilko, P., 2023. Topical delivery of mitogen-activated protein kinase inhibitor binimetinib prevents the development of cutaneous neurofibromas in neurofibromatosis type 1 mutant mice. Transl. Res. J. Lab. Clin. Med. 261, 16–27. https://doi.org/10.1016/j.trsl.2023.06.003

Davies, H., Bignell, G.R., Cox, C., Stephens, P., Edkins, S., Clegg, S., Teague, J., Woffendin, H., Garnett, M.J., Bottomley, W., Davis, N., Dicks, E., Ewing, R., Floyd, Y., Gray, K., Hall, S., Hawes, R., Hughes, J., Kosmidou, V., Menzies, A., Mould, C., Parker, A., Stevens, C., Watt, S., Hooper, S., Wilson, R., Jayatilake, H., Gusterson, B.A., Cooper, C., Shipley, J., Hargrave, D., Pritchard-Jones, K., Maitland, N., Chenevix-Trench, G., Riggins, G.J., Bigner, D.D., Palmieri, G., Cossu, A., Flanagan, A., Nicholson, A., Ho, J.W.C., Leung, S.Y., Yuen, S.T., Weber, B.L., Seigler, H.F., Darrow, T.L., Paterson, H., Marais, R., Marshall, C.J., Wooster, R., Stratton, M.R., Futreal, P.A., 2002. Mutations of the BRAF gene in human cancer. Nature 417, 949–954. https://doi.org/10.1038/nature00766

de Boode, W.P., Semmekrot, B.A., ter Laak, H.J., van der Burgt, C.J.A.M., Draaisma, J.M.T., Lommen, E.J.P., Sengers, R.C.A., van Wijk-Hoek, J.M., 1996. Myopathology in patients with a Noonan phenotype. Acta Neuropathol. (Berl.) 92, 597–602. https://doi.org/10.1007/s004010050566

De Ridder, W., van Engelen, B., van Alfen, N., 2022. Neurological features of Noonan syndrome and related RASopathies: Pain and nerve enlargement characterized by nerve ultrasound. Am. J. Med. Genet. A. 188, 1801–1807. https://doi.org/10.1002/ajmg.a.62714

DeRoos, S.T., Ryan, M.M., Ouvrier, R.A., 2007. Peripheral neuropathy in cardiofaciocutaneous syndrome. Pediatr. Neurol. 36, 250–252. https://doi.org/10.1016/j.pediatrneurol.2006.12.004

Dessars, B., De Raeve, L.E., Morandini, R., Lefort, A., El Housni, H., Ghanem, G.E., Van den Eynde, B.J., Ma, W., Roseeuw, D., Vassart, G., Libert, F., Heimann, P., 2009. Genotypic and Gene Expression Studies in Congenital Melanocytic Nevi: Insight into Initial Steps of Melanotumorigenesis. J. Invest. Dermatol. 129, 139–147. https://doi.org/10.1038/jid.2008.203

Dion, C., Roche, S., Laberthonnière, C., Broucqsault, N., Mariot, V., Xue, S., Gurzau, A.D., Nowak, A., Gordon, C.T., Gaillard, M.-C., El-Yazidi, C., Thomas, M., Schlupp-Robaglia, A., Missirian, C., Malan, V., Ratbi, L., Sefiani, A., Wollnik, B., Binetruy, B., Salort Campana, E., Attarian, S., Bernard, R., Nguyen, K., Amiel, J., Dumonceaux, J., Murphy, J.M., Déjardin, J., Blewitt, M.E., Reversade, B., Robin, J.D., Magdinier, F., 2019. SMCHD1 is involved in de novo methylation of the DUX4-encoding D4Z4 macrosatellite. Nucleic Acids Res. 47, 2822–2839. https://doi.org/10.1093/nar/gkz005

Dominguez, M.H., Ayoub, A.E., Rakic, P., 2013. POU-III Transcription Factors (Brn1, Brn2, and Oct6) Influence Neurogenesis, Molecular Identity, and Migratory Destination of Upper-Layer Cells of the Cerebral Cortex. Cereb. Cortex 23, 2632–2643. https://doi.org/10.1093/cercor/bhs252

Dong, X., Png, N.C.Y., Fortier, M.V., Lim, J.Y., Wong, K.P.L., Choo, J.T.L., Tan, E.C., Jamuar, S.S., 2022. Fibrous dysplasia in cardio-facio-cutaneous syndrome: A case report and review of literature. Am. J. Med. Genet. A. 188, 2732–2737. https://doi.org/10.1002/ajmg.a.62879

Draaisma, F., Erasmus, C.E., Braakman, H.M.H., Burgers, M.C.J., Leenders, E.K.S.M., Rinne, T., van Alfen, N., Draaisma, J.M.T., 2023a. Hypertrophic neuropathy: a possible cause of pain in children with Noonan syndrome and related disorders. Eur. J. Pediatr. 182, 3789–3793. https://doi.org/10.1007/s00431-023-05045-6

Draaisma, F., Erasmus, C.E., Braakman, H.M.H., Burgers, M.C.J., Leenders, E.K.S.M., Rinne, T., van Alfen, N., Draaisma, J.M.T., 2023b. Hypertrophic neuropathy: a possible cause of pain in children with Noonan syndrome and related disorders. Eur. J. Pediatr. 182, 3789–3793. https://doi.org/10.1007/s00431-023-05045-6

Eerola, I., Boon, L.M., Mulliken, J.B., Burrows, P.E., Dompmartin, A., Watanabe, S., Vanwijck, R., Vikkula, M., 2003. Capillary malformation-arteriovenous malformation, a new clinical and genetic disorder caused by RASA1 mutations. Am. J. Hum. Genet. 73, 1240–9. https://doi.org/10.1086/379793

Etchevers, H.C., Dupin, E., Le Douarin, N.M., 2019a. The diverse neural crest: from embryology to human pathology. Development 146. https://doi.org/10.1242/dev.169821

Etchevers, H.C., Dupin, E., Le Douarin, N.M., 2019b. The diverse neural crest: from embryology to human pathology. Dev. Camb. Engl. 146, dev169821. https://doi.org/10.1242/dev.169821

Etchevers, H.C., Rose, C., Kahle, B., Vorbringer, H., Fina, F., Heux, P., Berger, I., Schwarz, B., Zaffran, S., Macagno, N., Krengel, S., 2018. Giant congenital melanocytic nevus with vascular malformation and epidermal cysts associated with a somatic activating mutation in BRAF. Pigment Cell Melanoma Res. 31, 437–441. https://doi.org/10.1111/pcmr.12685

Evangelista, J.E., Xie, Z., Marino, G.B., Nguyen, N., Clarke, D.J.B., Ma'ayan, A., 2023. Enrichr-KG: bridging enrichment analysis across multiple libraries. Nucleic Acids Res. 51, W168–W179. https://doi.org/10.1093/nar/gkad393

Feltri, M.L., D'Antonio, M., Previtali, S., Fasolini, M., Messing, A., Wrabetz, L., 1999. P0-Cre transgenic mice for inactivation of adhesion molecules in Schwann cells. Ann. N. Y. Acad. Sci. 883, 116–123.

Feng, B., Li, X., Zhang, Q., Wang, Y., Gu, S., Yao, R., Li, Z., Gao, S., Chang, G., Li, Q., Li, N., Fu, L., Wang, J., Wang, X., 2023. Molecular and phenotypic spectrum of cardio-facio-cutaneous syndrome in Chinese patients. Orphanet J. Rare Dis. 18, 284. https://doi.org/10.1186/s13023-023-02878-0

Fledrich, R., Akkermann, D., Schütza, V., Abdelaal, T.A., Hermes, D., Schäffner, E., Soto-Bernardini, M.C., Götze, T., Klink, A., Kusch, K., Krueger, M., Kungl, T., Frydrychowicz, C., Möbius, W., Brück, W., Mueller, W.C., Bechmann, I., Sereda, M.W., Schwab, M.H., Nave, K.-A., Stassart, R.M., 2019. NRG1 type I dependent autoparacrine stimulation of Schwann cells in onion bulbs of peripheral neuropathies. Nat. Commun. 10, 1467. https://doi.org/10.1038/s41467-019-09385-6

Furlan, A., Dyachuk, V., Kastriti, M.E., Calvo-Enrique, L., Abdo, H., Hadjab, S., Chontorotzea, T., Akkuratova, N., Usoskin, D., Kamenev, D., Petersen, J., Sunadome, K., Memic, F., Marklund, U., Fried, K., Topilko, P., Lallemend, F., Kharchenko, P.V., Ernfors, P., Adameyko, I., 2017. Multipotent peripheral glial cells generate neuroendocrine cells of the adrenal medulla. Science 357, eaal3753. https://doi.org/10.1126/science.aal3753

Garnett, M.J., Marais, R., 2004. Guilty as charged: B-RAF is a human oncogene. Cancer Cell 6, 313–319. https://doi.org/10.1016/j.ccr.2004.09.022

Garratt, A.N., Voiculescu, O., Topilko, P., Charnay, P., Birchmeier, C., 2000. A dual role of erbB2 in myelination and in expansion of the schwann cell precursor pool. J. Cell Biol. 148, 1035–1046. https://doi.org/10.1083/jcb.148.5.1035

Gerschenfeld, G., Coulpier, F., Gresset, A., Pulh, P., Job, B., Topilko, T., Siegenthaler, J., Kastriti, M.E., Brunet, I., Charnay, P., Topilko, P., 2023. Neural tube-associated boundary caps are a major source of mural cells in the skin. eLife 12, e69413. https://doi.org/10.7554/eLife.69413

Gresset, A., Coulpier, F., Gerschenfeld, G., Jourdon, A., Matesic, G., Richard, L., Vallat, J.M., Charnay, P., Topilko, P., 2015. Boundary Caps Give Rise to Neurogenic Stem Cells and Terminal Glia in the Skin. Stem Cell Rep. 5, 278–290. https://doi.org/10.1016/j.stemcr.2015.06.005

Gripp, K.W., Lin, A.E., Nicholson, L., Allen, W., Cramer, A., Jones, K.L., Kutz, W., Peck, D., Rebolledo, M.A., Wheeler, P.G., Wilson, W., Al-Rahawan, M.M., Stabley, D.L., Sol-Church, K., 2007. Further delineation of the phenotype resulting from BRAF or MEK1 germline mutations helps differentiate cardio-facio-cutaneous syndrome from Costello syndrome. Am. J. Med. Genet. A. 143A, 1472–1480. https://doi.org/10.1002/ajmg.a.31815

Grissa, D., Junge, A., Oprea, T.I., Jensen, L.J., 2022. Diseases 2.0: a weekly updated database of disease–gene associations from text mining and data integration. Database 2022, baac019. https://doi.org/10.1093/database/baac019

Gualtieri, A., Kyprianou, N., Gregory, L.C., Vignola, M.L., Nicholson, J.G., Tan, R., Inoue, S., Scagliotti, V., Casado, P., Blackburn, J., Abollo-Jimenez, F., Marinelli, E., Besser, R.E.J., Högler, W., Karen Temple, I., Davies, J.H., Gagunashvili, A., Robinson, I.C.A.F., Camper, S.A., Davis, S.W., Cutillas, P.R., Gevers, E.F., Aoki, Y., Dattani, M.T., Gaston-Massuet, C., 2021. Activating mutations in BRAF disrupt the hypothalamo-pituitary axis leading to hypopituitarism in mice and humans. Nat. Commun. 12, 2028. https://doi.org/10.1038/s41467-021-21712-4

Guo, J., Yang, T., Zhang, W., Yu, K., Xu, X., Li, W., Song, L., Gu, X., Cao, R., Cui, S., 2024. Inhibition of CD44 suppresses the formation of fibrotic scar after spinal cord injury via the JAK2/STAT3 signaling pathway. iScience 27, 108935. https://doi.org/10.1016/j.isci.2024.108935

Hafner, C., Groesser, L., 2013. Mosaic RASopathies. Cell Cycle 12, 43–50. https://doi.org/10.4161/cc.23108

Hagedorn, L., Suter, U., Sommer, L., 1999. P0 and PMP22 mark a multipotent neural crest-derived cell type that displays community effects in response to TGF-beta family factors. Dev. Camb. Engl. 126, 3781–3794. https://doi.org/10.1242/dev.126.17.3781

Harrisingh, M.C., Perez-Nadales, E., Parkinson, D.B., Malcolm, D.S., Mudge, A.W., Lloyd, A.C., 2004. The Ras/Raf/ERK signalling pathway drives Schwann cell dedifferentiation. EMBO J. 23, 3061–3071. https://doi.org/10.1038/sj.emboj.7600309

Hashimoto, M., Ishii, K., Nakamura, Y., Watabe, K., Kohsaka, S., Akazawa, C., 2008. Neuroprotective effect of sonic hedgehog up-regulated in Schwann cells following sciatic nerve injury. J. Neurochem. 107, 918–927. https://doi.org/10.1111/j.1471-4159.2008.05666.x

Hernández-Porras, I., Fabbiano, S., Schuhmacher, A.J., Aicher, A., Cañamero, M., Cámara, J.A., Cussó, L., Desco, M., Heeschen, C., Mulero, F., Bustelo, X.R., Guerra, C., Barbacid, M., 2014. K-RasV14I recapitulates Noonan syndrome in mice. Proc. Natl. Acad. Sci. U. S. A. 111, 16395–16400. https://doi.org/10.1073/pnas.1418126111

Hörner, S.J., Couturier, N., Bruch, R., Koch, P., Hafner, M., Rudolf, R., 2021a. hiPSC-Derived Schwann Cells Influence Myogenic Differentiation in Neuromuscular Cocultures. Cells 10, 3292. https://doi.org/10.3390/cells10123292

Hörner, S.J., Couturier, N., Bruch, R., Koch, P., Hafner, M., Rudolf, R., 2021b. hiPSC-Derived Schwann Cells Influence Myogenic Differentiation in Neuromuscular Cocultures. Cells 10, 3292. https://doi.org/10.3390/cells10123292

Inoue, S.-I., Moriya, M., Watanabe, Y., Miyagawa-Tomita, S., Niihori, T., Oba, D., Ono, M., Kure, S., Ogura, T., Matsubara, Y., Aoki, Y., 2014. New BRAF knockin mice provide a pathogenetic mechanism of developmental defects and a therapeutic approach in cardio-facio-cutaneous syndrome. Hum. Mol. Genet. 23, 6553–6566. https://doi.org/10.1093/hmg/ddu376

Ishii, A., Furusho, M., Bansal, R., 2013. Sustained activation of ERK1/2 MAPK in oligodendrocytes and schwann cells enhances myelin growth and stimulates oligodendrocyte progenitor expansion. J. Neurosci. Off. J. Soc. Neurosci. 33, 175–186. https://doi.org/10.1523/JNEUROSCI.4403-12.2013

Ishii, A., Furusho, M., Dupree, J.L., Bansal, R., 2016. Strength of ERK1/2 MAPK Activation Determines Its Effect on Myelin and Axonal Integrity in the Adult CNS. J. Neurosci. Off. J. Soc. Neurosci. 36, 6471–6487. https://doi.org/10.1523/JNEUROSCI.0299-16.2016

Ito, N., Miyagoe-Suzuki, Y., Takeda, S., Kudo, A., 2021. Periostin Is Required for the Maintenance of Muscle Fibers during Muscle Regeneration. Int. J. Mol. Sci. 22, 3627. https://doi.org/10.3390/ijms22073627

Jaegle, M., Ghazvini, M., Mandemakers, W., Piirsoo, M., Driegen, S., Levavasseur, F., Raghoenath, S., Grosveld, F., Meijer, D., 2003. The POU proteins Brn-2 and Oct-6 share important functions in Schwann cell development. Genes Dev. 17, 1380–1391. https://doi.org/10.1101/gad.258203

Jessen, K.R., Mirsky, R., 2008. Negative regulation of myelination: relevance for development, injury, and demyelinating disease. Glia 56, 1552–1565. https://doi.org/10.1002/glia.20761

Journal Officiel, F., 2021. LOI n° 2021-1017 du 2 août 2021 relative à la bioéthique.

Kaiser, T., Allen, H.M., Kwon, O., Barak, B., Wang, J., He, Z., Jiang, M., Feng, G., 2021. MyelTracer: A Semi-Automated Software for Myelin g-Ratio Quantification. eNeuro 8, ENEURO.0558-20.2021. https://doi.org/10.1523/ENEURO.0558-20.2021

Kang, M., Lee, Y.-S., 2019. The impact of RASopathy-associated mutations on CNS development in mice and humans. Mol. Brain 12, 96. https://doi.org/10.1186/s13041-019-0517-5

Kawakami, H., Huang, S., Pal, K., Dutta, S.K., Mukhopadhyay, D., Sinicrope, F.A., 2016. Mutant BRAF Upregulates MCL-1 to Confer Apoptosis Resistance that Is Reversed by MCL-1 Antagonism and Cobimetinib in Colorectal Cancer. Mol. Cancer Ther. 15, 3015–3027. https://doi.org/10.1158/1535-7163.MCT-16-0017

Kolberg, L., Raudvere, U., Kuzmin, I., Adler, P., Vilo, J., Peterson, H., 2023. g:Profiler—interoperable web service for functional enrichment analysis and gene identifier mapping (2023 update). Nucleic Acids Res. 51, W207–W212. https://doi.org/10.1093/nar/gkad347

Kratz, C.P., Rapisuwon, S., Reed, H., Hasle, H., Rosenberg, P.S., 2011. Cancer in Noonan, Costello, Cardiofaciocutaneous and LEOPARD Syndromes. Am. J. Med. Genet. C Semin. Med. Genet. 157, 83–89. https://doi.org/10.1002/ajmg.c.30300

Kurek, K.C., Luks, V.L., Ayturk, U.M., Alomari, A.I., Fishman, S.J., Spencer, S.A., Mulliken, J.B., Bowen, M.E., Yamamoto, G.L., Kozakewich, H.P.W., Warman, M.L., 2012. Somatic mosaic activating mutations in PIK3CA cause CLOVES syndrome. Am. J. Hum. Genet. 90, 1108–1115. https://doi.org/10.1016/j.ajhg.2012.05.006

Le Douarin, N., Dulac, C., Dupin, E., Cameron-Curry, P., 1991. Glial cell lineages in the neural crest. Glia 4, 175–84. https://doi.org/10.1002/glia.440040209

Le, N., Nagarajan, R., Wang, J.Y.T., Araki, T., Schmidt, R.E., Milbrandt, J., 2005a. Analysis of congenital hypomyelinating Egr2Lo/Lo nerves identifies Sox2 as an inhibitor of Schwann cell differentiation and myelination. Proc. Natl. Acad. Sci. U. S. A. 102, 2596–2601. https://doi.org/10.1073/pnas.0407836102

Le, N., Nagarajan, R., Wang, J.Y.T., Araki, T., Schmidt, R.E., Milbrandt, J., 2005b. Analysis of congenital hypomyelinating Egr2Lo/Lo nerves identifies Sox2 as an inhibitor of Schwann cell differentiation and myelination. Proc. Natl. Acad. Sci. U. S. A. 102, 2596–2601. https://doi.org/10.1073/pnas.0407836102

Liao, Y., Wang, J., Jaehnig, E.J., Shi, Z., Zhang, B., 2019. WebGestalt 2019: gene set analysis toolkit with revamped UIs and APIs. Nucleic Acids Res. 47, W199–W205. https://doi.org/10.1093/nar/gkz401

Lin, H.-P., Oksuz, I., Hurley, E., Wrabetz, L., Awatramani, R., 2015. Microprocessor complex subunit DiGeorge syndrome critical region gene 8 (Dgcr8) is required for schwann cell

myelination and myelin maintenance. J. Biol. Chem. 290, 24294–24307. https://doi.org/10.1074/jbc.M115.636407
Lindhurst, M.J., Parker, V.E.R., Payne, F., Sapp, J.C., Rudge, S., Harris, J., Witkowski, A.M., Zhang, Q., Groeneveld, M.P., Scott, C.E., Daly, A., Huson, S.M., Tosi, L.L., Cunningham, M.L., Darling, T.N., Geer, J., Gucev, Z., Sutton, V.R., Tziotzios, C., Dixon, A.K., Helliwell, T., O'Rahilly, S., Savage, D.B., Wakelam, M.J.O., Barroso, I., Biesecker, L.G., Semple, R.K., 2012. Mosaic overgrowth with fibroadipose hyperplasia is caused by somatic activating mutations in PIK3CA. Nat. Genet. 44, 928–933. https://doi.org/10.1038/ng.2332
Liu, D., Liu, Z., Condouris, S., Xing, M., 2007. BRAF V600E maintains proliferation, transformation, and tumorigenicity of BRAF-mutant papillary thyroid cancer cells. J. Clin. Endocrinol. Metab. 92, 2264–2271. https://doi.org/10.1210/jc.2006-1613
Lorts, A., Schwanekamp, J.A., Baudino, T.A., McNally, E.M., Molkentin, J.D., 2012. Deletion of periostin reduces muscular dystrophy and fibrosis in mice by modulating the transforming growth factor-β pathway. Proc. Natl. Acad. Sci. 109, 10978–10983. https://doi.org/10.1073/pnas.1204708109
Maeda, Y., Tidyman, W.E., Ander, B.P., Pritchard, C.A., Rauen, K.A., 2021. Ras/MAPK dysregulation in development causes a skeletal myopathy in an activating BrafL597V mouse model for cardio-facio-cutaneous syndrome. Dev. Dyn. 250, 1074–1095. https://doi.org/10.1002/dvdy.309
Maldonado, E.N., Alderson, N.L., Monje, P.V., Wood, P.M., Hama, H., 2008. FA2H is responsible for the formation of 2-hydroxy galactolipids in peripheral nervous system myelin. J. Lipid Res. 49, 153–161. https://doi.org/10.1194/jlr.M700400-JLR200
Manci, E.A., Martinez, J.E., Horenstein, M.G., Gardner, T.M., Ahmed, A., Mancao, M.C., Gremse, D.A., Gardner, D.M., Nimityongskul, P., Maertens, P., Riddick, L., Kavamura, M.I., 2005. Cardiofaciocutaneous syndrome (CFC) with congenital peripheral neuropathy and nonorganic malnutrition: an autopsy study. Am. J. Med. Genet. A. 137, 1–8. https://doi.org/10.1002/ajmg.a.30834
Marechal, E., Poliard, A., Henry, K., Moreno, M., Legrix, M., Macagno, N., Mondielli, G., Fauquier, T., Barlier, A., Etchevers, H.C., 2022. Multiple congenital malformations arise from somatic mosaicism for constitutively active Pik3ca signaling. Front. Cell Dev. Biol., Women in Signaling 10, 1013001. https://doi.org/10.3389/fcell.2022.1013001
Maridet, C., Sole, G., Morice-Picard, F., Taieb, A., 2016. Hypertrophic neuropathy in Noonan syndrome with multiple lentigines. Am. J. Med. Genet. A. 170, 1570–1572. https://doi.org/10.1002/ajmg.a.37601
Maro, G.S., Vermeren, M., Voiculescu, O., Melton, L., Cohen, J., Charnay, P., Topilko, P., 2004. Neural crest boundary cap cells constitute a source of neuronal and glial cells of the PNS. Nat. Neurosci. 7, 930–938. https://doi.org/10.1038/nn1299
McCowan, J., Fercoq, F., Kirkwood, P.M., T'Jonck, W., Hegarty, L.M., Mawer, C.M., Cunningham, R., Mirchandani, A.S., Hoy, A., Humphries, D.C., Jones, G.-R., Hansen, C.G., Hirani, N., Jenkins, S.J., Henri, S., Malissen, B., Walmsley, S.R., Dockrell, D.H., Saunders, P.T.K., Carlin, L.M., Bain, C.C., 2021. The transcription factor EGR2 is indispensable for tissue-specific imprinting of alveolar macrophages in health and tissue repair. Sci. Immunol. 6, eabj2132. https://doi.org/10.1126/sciimmunol.abj2132
Mercer, K., Giblett, S., Green, S., Lloyd, D., DaRocha Dias, S., Plumb, M., Marais, R., Pritchard, C., 2005. Expression of endogenous oncogenic V600EB-raf induces proliferation and developmental defects in mice and transformation of primary fibroblasts. Cancer Res. 65, 11493–11500. https://doi.org/10.1158/0008-5472.CAN-05-2211
Meyer, D., Birchmeier, C., 1995. Multiple essential functions of neuregulin in development. Nature 378, 386–390. https://doi.org/10.1038/378386a0
Mirzaa, G., Timms, A.E., Conti, V., Boyle, E.A., Girisha, K.M., Martin, B., Kircher, M., Olds, C., Juusola, J., Collins, S., Park, K., Carter, M., Glass, I., Krägeloh-Mann, I., Chitayat, D., Parikh, A.S., Bradshaw, R., Torti, E., Braddock, S., Burke, L., Ghedia, S.,

Stephan, M., Stewart, F., Prasad, C., Napier, M., Saitta, S., Straussberg, R., Gabbett, M., O'Connor, B.C., Keegan, C.E., Yin, L.J., Lai, A.H.M., Martin, N., McKinnon, M., Addor, M.-C., Boccuto, L., Schwartz, C.E., Lanoel, A., Conway, R.L., Devriendt, K., Tatton-Brown, K., Pierpont, M.E., Painter, M., Worgan, L., Reggin, J., Hennekam, R., Tsuchiya, K., Pritchard, C.C., Aracena, M., Gripp, K.W., Cordisco, M., Van Esch, H., Garavelli, L., Curry, C., Goriely, A., Kayserilli, H., Shendure, J., Graham, J., Guerrini, R., Dobyns, W.B., 2016. PIK3CA-associated developmental disorders exhibit distinct classes of mutations with variable expression and tissue distribution. JCI Insight 1, e87623, 87623. https://doi.org/10.1172/jci.insight.87623

Moriya, M., Inoue, S., Miyagawa-Tomita, S., Nakashima, Y., Oba, D., Niihori, T., Hashi, M., Ohnishi, H., Kure, S., Matsubara, Y., Aoki, Y., 2015. Adult mice expressing a Braf Q241R mutation on an ICR/CD-1 background exhibit a cardio-facio-cutaneous syndrome phenotype. Hum. Mol. Genet. 24, 7349–7360. https://doi.org/10.1093/hmg/ddv435

Morren, M.-A., Fodstad, H., Brems, H., Bedoni, N., Guenova, E., Jacot-Guillarmod, M., Busiah, K., Giuliano, F., Gilliet, M., Atallah, I., 2024. Mosaic RASopathies concept: different skin lesions, same systemic manifestations? J. Med. Genet. jmg-2023-109306. https://doi.org/10.1136/jmg-2023-109306

Moss, K.R., Bopp, T.S., Johnson, A.E., Höke, A., 2021. New Evidence for Secondary Axonal Degeneration in Demyelinating Neuropathies. Neurosci. Lett. 744, 135595. https://doi.org/10.1016/j.neulet.2020.135595

Napoli, I., Noon, L.A., Ribeiro, S., Kerai, A.P., Parrinello, S., Rosenberg, L.H., Collins, M.J., Harrisingh, M.C., White, I.J., Woodhoo, A., Lloyd, A.C., 2012. A central role for the ERK-signaling pathway in controlling Schwann cell plasticity and peripheral nerve regeneration in vivo. Neuron 73, 729–742. https://doi.org/10.1016/j.neuron.2011.11.031

Nava, C., Hanna, N., Michot, C., Pereira, S., Pouvreau, N., Niihori, T., Aoki, Y., Matsubara, Y., Arveiler, B., Lacombe, D., Pasmant, E., Parfait, B., Baumann, C., Héron, D., Sigaudy, S., Toutain, A., Rio, M., Goldenberg, A., Leheup, B., Verloes, A., Cavé, H., 2007. Cardio-facio-cutaneous and Noonan syndromes due to mutations in the RAS/MAPK signalling pathway: genotype-phenotype relationships and overlap with Costello syndrome. J. Med. Genet. 44, 763–771. https://doi.org/10.1136/jmg.2007.050450

Nave, K.-A., Salzer, J.L., 2006. Axonal regulation of myelination by neuregulin 1. Curr. Opin. Neurobiol. 16, 492–500. https://doi.org/10.1016/j.conb.2006.08.008

Newbern, J., Birchmeier, C., 2010. Nrg1/ErbB signaling networks in Schwann cell development and myelination. Semin. Cell Dev. Biol. 21, 922–928. https://doi.org/10.1016/j.semcdb.2010.08.008

Newbern, J.M., Li, X., Shoemaker, S.E., Zhou, J., Zhong, J., Wu, Y., Bonder, D., Hollenback, S., Coppola, G., Geschwind, D.H., Landreth, G.E., Snider, W.D., 2011. Specific functions for ERK/MAPK signaling during PNS development. Neuron 69, 91–105. https://doi.org/10.1016/j.neuron.2010.12.003

Nusinow, D.P., Szpyt, J., Ghandi, M., Rose, C.M., McDonald, E.R., Kalocsay, M., Jané-Valbuena, J., Gelfand, E., Schweppe, D.K., Jedrychowski, M., Golji, J., Porter, D.A., Rejtar, T., Wang, Y.K., Kryukov, G.V., Stegmeier, F., Erickson, B.K., Garraway, L.A., Sellers, W.R., Gygi, S.P., 2020. Quantitative Proteomics of the Cancer Cell Line Encyclopedia. Cell 180, 387-402.e16. https://doi.org/10.1016/j.cell.2019.12.023

Office for Human Research Protections, (OHRP), 2018. The Belmont Report [WWW Document]. Ethical Princ. Guidel. Prot. Hum. Subj. Res. URL https://www.hhs.gov/ohrp/regulations-and-policy/belmont-report/read-the-belmont-report/index.html (accessed 3.26.24).

Ogata, T., Iijima, S., Hoshikawa, S., Miura, T., Yamamoto, S., Oda, H., Nakamura, K., Tanaka, S., 2004. Opposing extracellular signal-regulated kinase and Akt pathways control Schwann cell myelination. J. Neurosci. Off. J. Soc. Neurosci. 24, 6724–6732. https://doi.org/10.1523/JNEUROSCI.5520-03.2004

Ohashi, K., Osuga, J., Tozawa, R., Kitamine, T., Yagyu, H., Sekiya, M., Tomita, S., Okazaki, H., Tamura, Y., Yahagi, N., Iizuka, Y., Harada, K., Gotoda, T., Shimano, H., Yamada, N., Ishibashi, S., 2003. Early embryonic lethality caused by targeted disruption of the 3-hydroxy-3-methylglutaryl-CoA reductase gene. J. Biol. Chem. 278, 42936–42941. https://doi.org/10.1074/jbc.M307228200

Peirano, R.I., Goerich, D.E., Riethmacher, D., Wegner, M., 2000. Protein zero gene expression is regulated by the glial transcription factor Sox10. Mol. Cell. Biol. 20, 3198–3209. https://doi.org/10.1128/MCB.20.9.3198-3209.2000

Piirsoo, M., Kaljas, A., Tamm, K., Timmusk, T., 2010. Expression of NGF and GDNF family members and their receptors during peripheral nerve development and differentiation of Schwann cells in vitro. Neurosci. Lett. 469, 135–140. https://doi.org/10.1016/j.neulet.2009.11.060

Poitelon, Y., Kopec, A.M., Belin, S., 2020. Myelin Fat Facts: An Overview of Lipids and Fatty Acid Metabolism. Cells 9, 812. https://doi.org/10.3390/cells9040812

Pugliese, A., Della Marina, A., de Paula Estephan, E., Zanoteli, E., Roos, A., Schara-Schmidt, U., Hentschel, A., Azuma, Y., Töpf, A., Thompson, R., Polavarapu, K., Lochmüller, H., 2024. Mutations in PTPN11 could lead to a congenital myasthenic syndrome phenotype: a Noonan syndrome case series. J. Neurol. 271, 1331–1341. https://doi.org/10.1007/s00415-023-12070-w

Ramesh, R., Shaw, N., Miles, E.K., Richard, B., Colmenero, I., Moss, C., 2017. Mosaic NRAS Q61R mutation in a child with giant congenital melanocytic naevus, epidermal naevus syndrome and hypophosphataemic rickets | Clinical and Experimental Dermatology | Oxford Academic. Clin. Exp. Dermatol. 42, 75–79. https://doi.org/10.1111/ced.12969

Rauen, K.A., 2013a. The RASopathies. Annu. Rev. Genomics Hum. Genet. 14, 355–369. https://doi.org/10.1146/annurev-genom-091212-153523

Rauen, K.A., 2013b. The RASopathies. Annu. Rev. Genomics Hum. Genet. 14, 355–369. https://doi.org/10.1146/annurev-genom-091212-153523

Rauen, K.A., 2007. Cardiofaciocutaneous Syndrome, in: Adam, M.P., Feldman, J., Mirzaa, G.M., Pagon, R.A., Wallace, S.E., Bean, L.J., Gripp, K.W., Amemiya, A. (Eds.), GeneReviews®. University of Washington, Seattle, Seattle (WA).

Riethmacher, D., Sonnenberg-Riethmacher, E., Brinkmann, V., Yamaai, T., Lewin, G.R., Birchmeier, C., 1997. Severe neuropathies in mice with targeted mutations in the ErbB3 receptor. Nature 389, 725–730. https://doi.org/10.1038/39593

Roberts, S.L., Dun, X., Doddrell, R.D.S., Mindos, T., Drake, L.K., Onaitis, M.W., Florio, F., Quattrini, A., Lloyd, A.C., D'Antonio, M., Parkinson, D.B., 2017. Sox2 expression in Schwann cells inhibits myelination in vivo and induces influx of macrophages to the nerve. Dev. Camb. Engl. 144, 3114–3125. https://doi.org/10.1242/dev.150656

Serra-Nédélec, A.D.R., Edouard, T., Tréguer, K., Tajan, M., Araki, T., Dance, M., Mus, M., Montagner, A., Tauber, M., Salles, J.-P., Valet, P., Neel, B.G., Raynal, P., Yart, A., 2012. Noonan syndrome-causing SHP2 mutants inhibit insulin-like growth factor 1 release via growth hormone-induced ERK hyperactivation, which contributes to short stature. Proc. Natl. Acad. Sci. 109, 4257–4262. https://doi.org/10.1073/pnas.1119803109

Sheean, M.E., McShane, E., Cheret, C., Walcher, J., Müller, T., Wulf-Goldenberg, A., Hoelper, S., Garratt, A.N., Krüger, M., Rajewsky, K., Meijer, D., Birchmeier, W., Lewin, G.R., Selbach, M., Birchmeier, C., 2014. Activation of MAPK overrides the termination of myelin growth and replaces Nrg1/ErbB3 signals during Schwann cell development and myelination. Genes Dev. 28, 290–303. https://doi.org/10.1101/gad.230045.113

Sheu, J.Y., Kulhanek, D.J., Eckenstein, F.P., 2000. Differential patterns of ERK and STAT3 phosphorylation after sciatic nerve transection in the rat. Exp. Neurol. 166, 392–402. https://doi.org/10.1006/exnr.2000.7508

Siano, M.A., Pivonello, R., Salerno, M., Falco, M., Mauro, C., De Brasi, D., Klain, A., Sestito, S., De Luca, A., Pinna, V., Simeoli, C., Concolino, D., Mainolfi, C.G., Mannarino, T.,

Strisciuglio, P., Tartaglia, M., Melis, D., 2022. Endocrine system involvement in patients with RASopathies: A case series. Front. Endocrinol. 13. https://doi.org/10.3389/fendo.2022.1030398

Souza, J.F., Passos, R.L.F., Guedes, A.C.M., Rezende, N.A., Rodrigues, L.O.C., 2009. Muscular force is reduced in neurofibromatosis type 1. J. Musculoskelet. Neuronal Interact. 9, 15–17.

Stassart, R.M., Fledrich, R., Velanac, V., Brinkmann, B.G., Schwab, M.H., Meijer, D., Sereda, M.W., Nave, K.-A., 2013. A role for Schwann cell-derived neuregulin-1 in remyelination. Nat. Neurosci. 16, 48–54. https://doi.org/10.1038/nn.3281

Stevenson, D.A., Allen, S., Tidyman, W.E., Carey, J.C., Viskochil, D.H., Stevens, A., Hanson, H., Sheng, X., Thompson, B.A., J. Okumura, M., Reinker, K., Johnson, B., Rauen, K.A., 2012. Peripheral muscle weakness in RASopathies. Muscle Nerve 46, 394–399. https://doi.org/10.1002/mus.23324

Subramanian, A., Tamayo, P., Mootha, V.K., Mukherjee, S., Ebert, B.L., Gillette, M.A., Paulovich, A., Pomeroy, S.L., Golub, T.R., Lander, E.S., Mesirov, J.P., 2005. Gene set enrichment analysis: A knowledge-based approach for interpreting genome-wide expression profiles. Proc. Natl. Acad. Sci. 102, 15545–15550. https://doi.org/10.1073/pnas.0506580102

Tartaglia, M., Gelb, B.D., Zenker, M., 2011. Noonan syndrome and clinically related disorders. Best Pract. Res. Clin. Endocrinol. Metab. 25, 161–179. https://doi.org/10.1016/j.beem.2010.09.002

The World Medical Association, (WMA), 2022. WMA Declaration of Helsinki [WWW Document]. Ethical Princ. Med. Res. Involv. Hum. Subj. URL https://www.wma.net/policies-post/wma-declaration-of-helsinki-ethical-principles-for-medical-research-involving-human-subjects/ (accessed 3.26.24).

Themistocleous, A.C., Ramirez, J.D., Serra, J., Bennett, D.L.H., 2014. The clinical approach to small fibre neuropathy and painful channelopathy. Pract. Neurol. 14, 368–379. https://doi.org/10.1136/practneurol-2013-000758

Thomas, S., Thomas, M., Wincker, P., Babarit, C., Xu, P., Speer, M.C., Munnich, A., Lyonnet, S., Vekemans, M., Etchevers, H.C., 2008. Human neural crest cells display molecular and phenotypic hallmarks of stem cells. Hum. Mol. Genet. 17, 3411–3425. https://doi.org/10.1093/hmg/ddn235

Tian, Z., Du, Z., Bai, G., Gong, Q., You, Y., Xu, G., Liu, J., Xiao, M., Wang, Y., He, Y., 2024. Schwann cell derived pleiotrophin stimulates fibroblast for proliferation and excessive collagen deposition in plexiform neurofibroma. Cancer Gene Ther. 31, 627–640. https://doi.org/10.1038/s41417-024-00727-1

Timmerman, V., De Jonghe, P., Ceuterick, C., De Vriendt, E., Löfgren, A., Nelis, E., Warner, L.E., Lupski, J.R., Martin, J.J., Van Broeckhoven, C., 1999. Novel missense mutation in the early growth response 2 gene associated with Dejerine-Sottas syndrome phenotype. Neurology 52, 1827–1832. https://doi.org/10.1212/wnl.52.9.1827

Topilko, P., Schneider-Maunoury, S., Levi, G., Baron-Van Evercooren, A., Chennoufi, A.B., Seitanidou, T., Babinet, C., Charnay, P., 1994. Krox-20 controls myelination in the peripheral nervous system. Nature 371, 796–799. https://doi.org/10.1038/371796a0

Urosevic, J., Sauzeau, V., Soto-Montenegro, M.L., Reig, S., Desco, M., Wright, E.M.B., Cañamero, M., Mulero, F., Ortega, S., Bustelo, X.R., Barbacid, M., 2011. Constitutive activation of B-Raf in the mouse germ line provides a model for human cardio-facio-cutaneous syndrome. Proc. Natl. Acad. Sci. U. S. A. 108, 5015–5020. https://doi.org/10.1073/pnas.1016933108

Velanac, V., Unterbarnscheidt, T., Hinrichs, W., Gummert, M.N., Fischer, T.M., Rossner, M.J., Trimarco, A., Brivio, V., Taveggia, C., Willem, M., Haass, C., Möbius, W., Nave, K.-A., Schwab, M.H., 2012. BACE1 Processing of NRG1 Type III Produces a Myelin-Inducing Signal but Is Not Essential for the Stimulation of Myelination. Glia 60, 203–217. https://doi.org/10.1002/glia.21255

Vizcaino, M.A., Belzberg, A., Ahlawat, S., Belakhoua, S., Chen, L., Staedtke, V., Rodriguez, F.J., 2020. Localized Hypertrophic Neuropathy as a Neoplastic Manifestation of

KRAS-Mediated RASopathy. J. Neuropathol. Exp. Neurol. 79, 647–651. https://doi.org/10.1093/jnen/nlaa034

Voiculescu, O., Charnay, P., Schneider-Maunoury, S., 2000. Expression pattern of a Krox-20/Cre knock-in allele in the developing hindbrain, bones, and peripheral nervous system. Genes. N. Y. N 2000 26, 123–126. https://doi.org/10.1002/(sici)1526-968x(200002)26:2<123::aid-gene7>3.0.co;2-o

Warner, L.E., Mancias, P., Butler, I.J., McDonald, C.M., Keppen, L., Koob, K.G., Lupski, J.R., 1998. Mutations in the early growth response 2 (EGR2) gene are associated with hereditary myelinopathies. Nat. Genet. 18, 382–384. https://doi.org/10.1038/ng0498-382

Warner, L.E., Svaren, J., Milbrandt, J., Lupski, J.R., 1999. Functional consequences of mutations in the early growth response 2 gene (EGR2) correlate with severity of human myelinopathies. Hum. Mol. Genet. 8, 1245–1251. https://doi.org/10.1093/hmg/8.7.1245

Wu, X., Simpson, J., Hong, J.H., Kim, K.-H., Thavarajah, N.K., Backx, P.H., Neel, B.G., Araki, T., 2011. MEK-ERK pathway modulation ameliorates disease phenotypes in a mouse model of Noonan syndrome associated with the Raf1(L613V) mutation. J. Clin. Invest. 121, 1009–1025. https://doi.org/10.1172/JCI44929

Xing, M., Westra, W.H., Tufano, R.P., Cohen, Y., Rosenbaum, E., Rhoden, K.J., Carson, K.A., Vasko, V., Larin, A., Tallini, G., Tolaney, S., Holt, E.H., Hui, P., Umbricht, C.B., Basaria, S., Ewertz, M., Tufaro, A.P., Califano, J.A., Ringel, M.D., Zeiger, M.A., Sidransky, D., Ladenson, P.W., 2005. BRAF mutation predicts a poorer clinical prognosis for papillary thyroid cancer. J. Clin. Endocrinol. Metab. 90, 6373–6379. https://doi.org/10.1210/jc.2005-0987

Yeh, E., Dao, D.Q., Wu, Z.Y., Kandalam, S.M., Camacho, F.M., Tom, C., Zhang, W., Krencik, R., Rauen, K.A., Ullian, E.M., Weiss, L.A., 2018. Patient-derived iPSCs show premature neural differentiation and neuron type-specific phenotypes relevant to neurodevelopment. Mol. Psychiatry 23, 1687–1698. https://doi.org/10.1038/mp.2017.238

Zhao, S., Mekbib, K.Y., van der Ent, M.A., Allington, G., Prendergast, A., Chau, J.E., Smith, H., Shohfi, J., Ocken, J., Duran, D., Furey, C.G., Hao, L.T., Duy, P.Q., Reeves, B.C., Zhang, J., Nelson-Williams, C., Chen, D., Li, B., Nottoli, T., Bai, S., Rolle, M., Zeng, X., Dong, W., Fu, P.-Y., Wang, Y.-C., Mane, S., Piwowarczyk, P., Fehnel, K.P., See, A.P., Iskandar, B.J., Aagaard-Kienitz, B., Moyer, Q.J., Dennis, E., Kiziltug, E., Kundishora, A.J., DeSpenza, T., Greenberg, A.B.W., Kidanemariam, S.M., Hale, A.T., Johnston, J.M., Jackson, E.M., Storm, P.B., Lang, S.-S., Butler, W.E., Carter, B.S., Chapman, P., Stapleton, C.J., Patel, A.B., Rodesch, G., Smajda, S., Berenstein, A., Barak, T., Erson-Omay, E.Z., Zhao, H., Moreno-De-Luca, A., Proctor, M.R., Smith, E.R., Orbach, D.B., Alper, S.L., Nicoli, S., Boggon, T.J., Lifton, R.P., Gunel, M., King, P.D., Jin, S.C., Kahle, K.T., 2023. Mutation of key signaling regulators of cerebrovascular development in vein of Galen malformations. Nat. Commun. 14, 7452. https://doi.org/10.1038/s41467-023-43062-z

Zhu, Q., Song, L., Peng, G., Sun, N., Chen, J., Zhang, T., Sheng, N., Tang, W., Qian, C., Qiao, Y., Tang, K., Han, J.-D.J., Li, J., Jing, N., 2014. The transcription factor Pou3f1 promotes neural fate commitment via activation of neural lineage genes and inhibition of external signaling pathways. eLife 3, e02224. https://doi.org/10.7554/eLife.02224

Figure 1

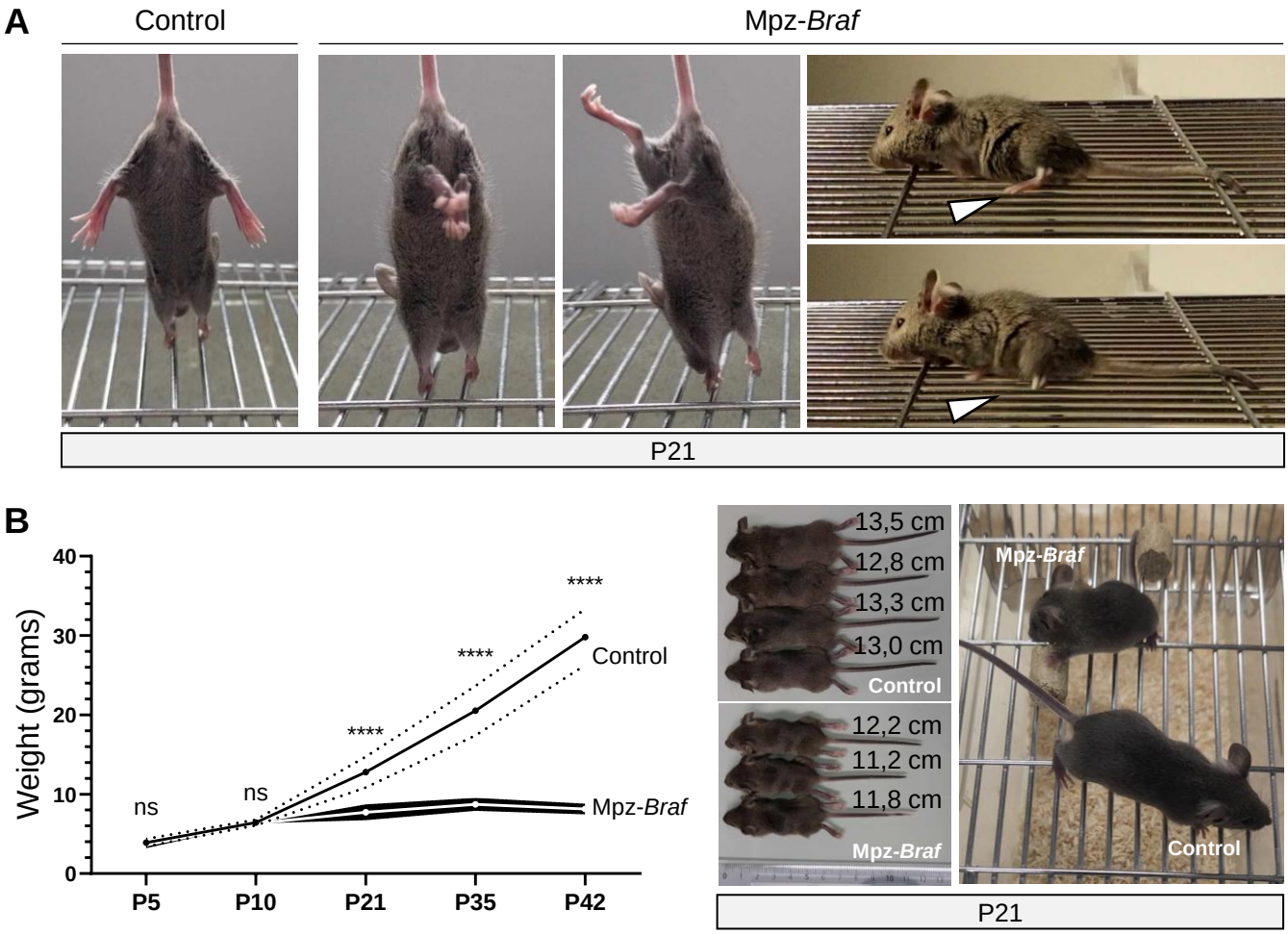
A
Control
Mpz-Braf
P21
B
Weight (grams)
40
30
20
10
0
ns
ns
****
****
****
Control
Mpz-Braf
P5
P10
P21
P35
P42
13,5 cm
12,8 cm
13,3 cm
13,0 cm
Control
12,2 cm
11,2 cm
11,8 cm
Mpz-Braf
Mpz-Braf
Control
P21

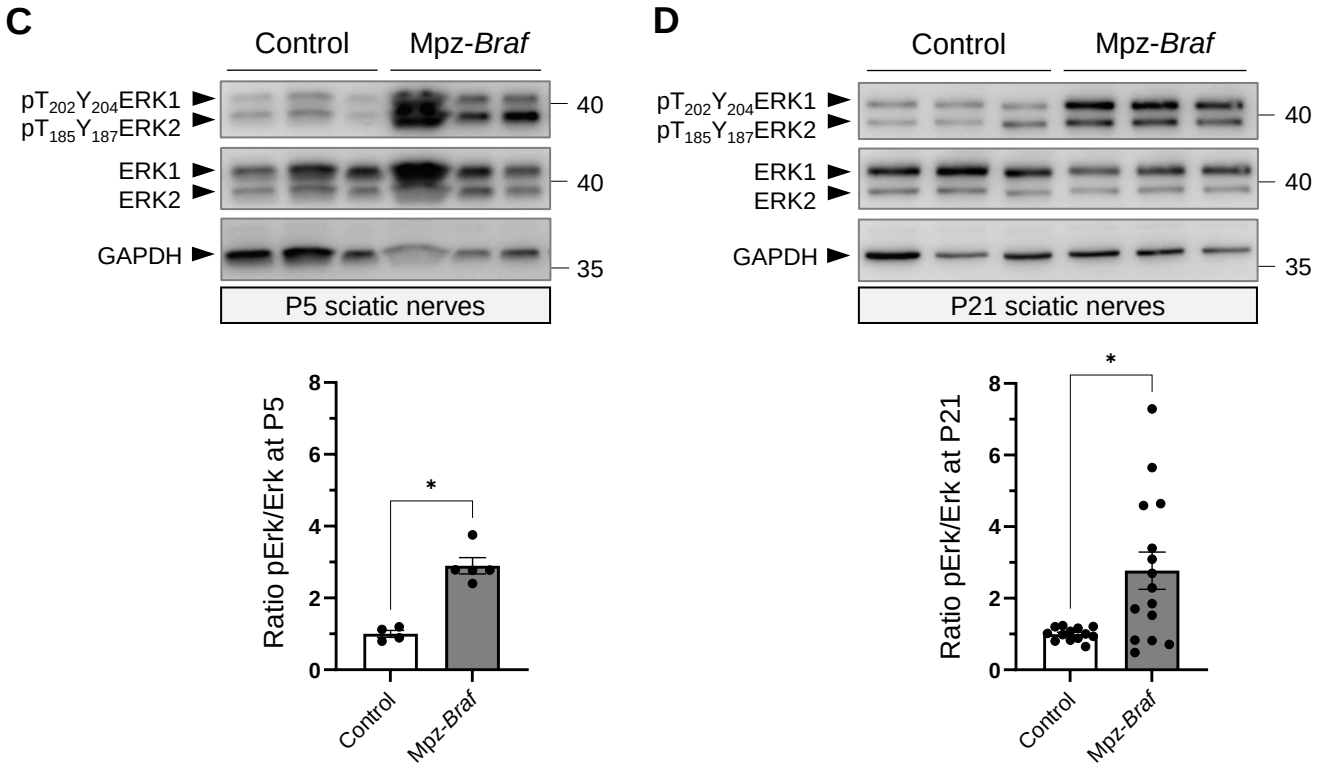
C
Control
Mpz-Braf
pT202Y204ERK1
pT185Y187ERK2
ERK1
ERK2
GAPDH
40
40
35
P5 sciatic nerves
Ratio pErk/Erk at P5
8
6
4
2
0
*
Control
Mpz-Braf
D
Control
Mpz-Braf
pT202Y204ERK1
pT185Y187ERK2
ERK1
ERK2
GAPDH
40
40
35
P21 sciatic nerves
Ratio pErk/Erk at P21
8
6
4
2
0
*
Control
Mpz-Braf

Figure 2

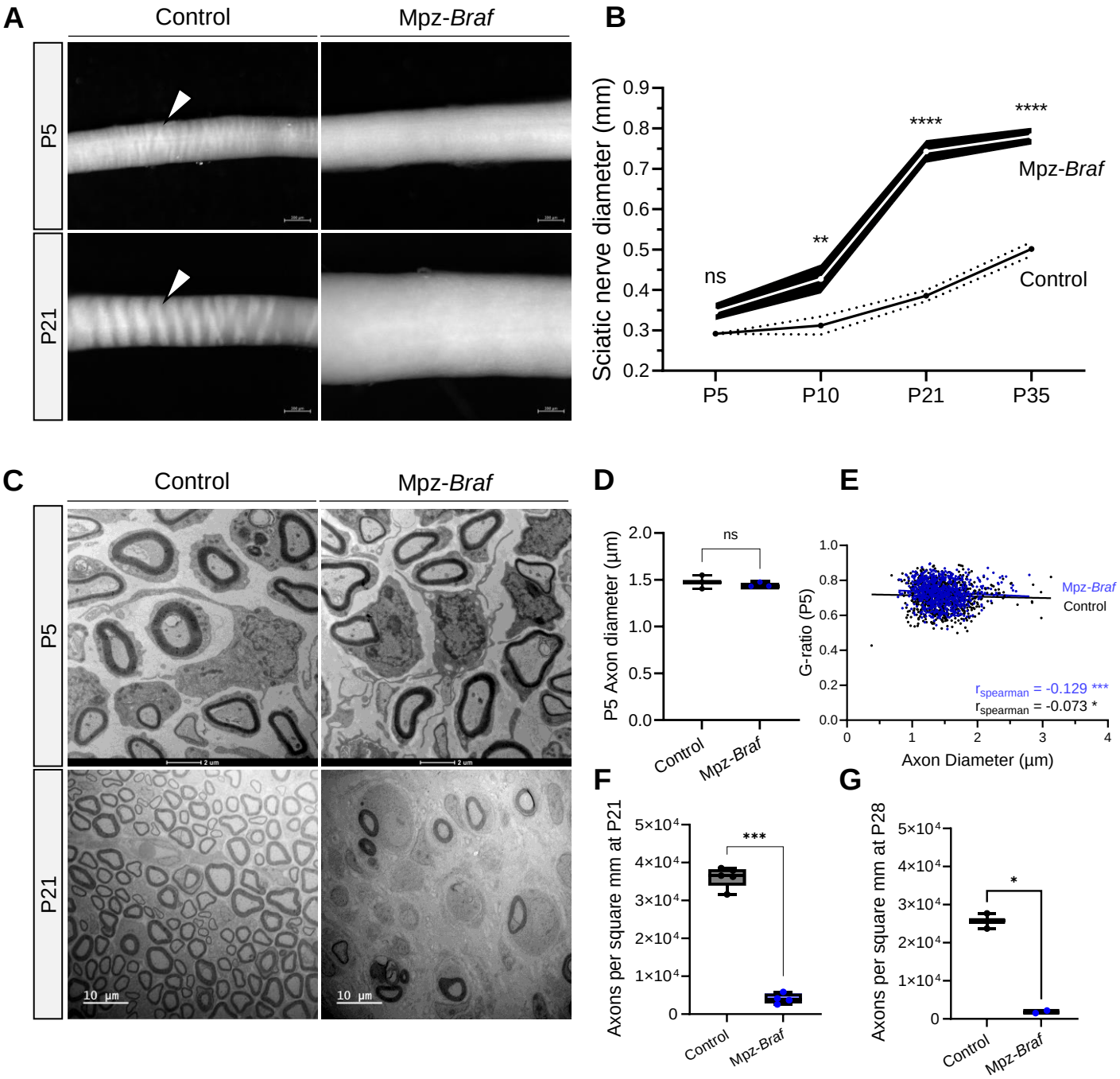
A
Control
Mpz-Braf
P5
P21
B
Sciatic nerve diameter (mm)
0.9
0.8
0.7
0.6
0.5
0.4
0.3
0.2
ns
**
****
****
Mpz-Braf
Control
P5
P10
P21
P35
C
Control
Mpz-Braf
P5
P21
10 µm
10 µm
D
P5 Axon diameter (µm)
2.0
1.5
1.0
0.5
0.0
ns
Control
Mpz-Braf
E
G-ratio (P5)
1.0
0.8
0.6
0.4
0.2
0.0
Mpz-Braf
Control
r spearman = -0.129 ***
r spearman = -0.073 *
0
1
2
3
4
Axon Diameter (µm)
F
Axons per square mm at P21
5×10⁴
4×10⁴
3×10⁴
2×10⁴
1×10⁴
0
***
Control
Mpz-Braf
G
Axons per square mm at P28
5×10⁴
4×10⁴
3×10⁴
2×10⁴
1×10⁴
0
*
Control
Mpz-Braf

Figure 3

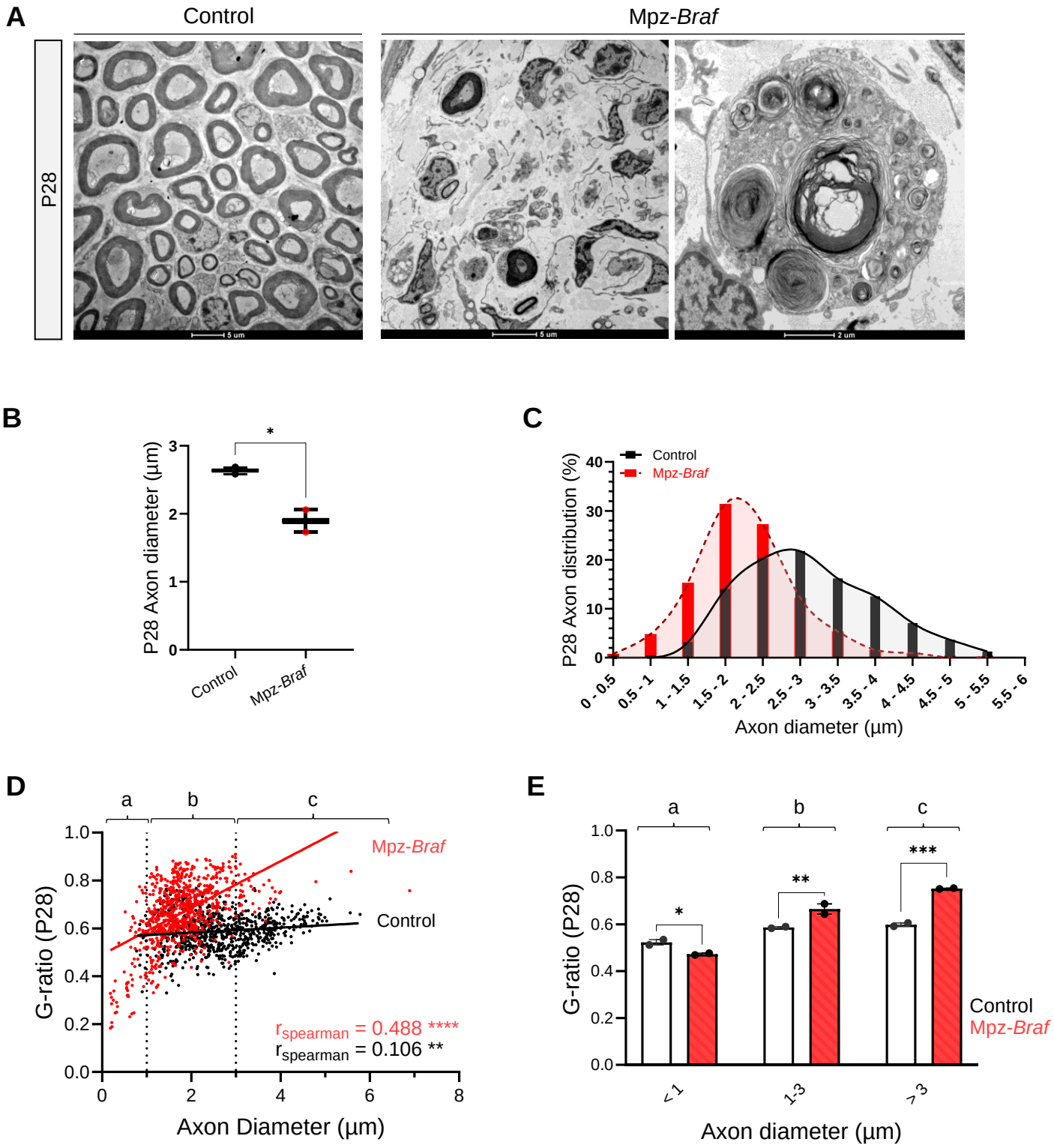
A
Control
Mpz-Braf
P28
5 um
5 um
2 um
B
P28 Axon diameter (µm)
*
Control
Mpz-Braf
C
Control
Mpz-Braf
P28 Axon distribution (%)
0 - 0.5
0.5 - 1
1 - 1.5
1.5 - 2
2 - 2.5
2.5 - 3
3 - 3.5
3.5 - 4
4 - 4.5
4.5 - 5
5 - 5.5
5.5 - 6
Axon diameter (µm)
D
a
b
c
Mpz-Braf
Control
G-ratio (P28)
r spearman = 0.488 ****
r spearman = 0.106 **
Axon Diameter (µm)
E
a
b
c
*
**
***
G-ratio (P28)
Control
Mpz-Braf
<1
1-3
>3
Axon diameter (µm)

Figure 4

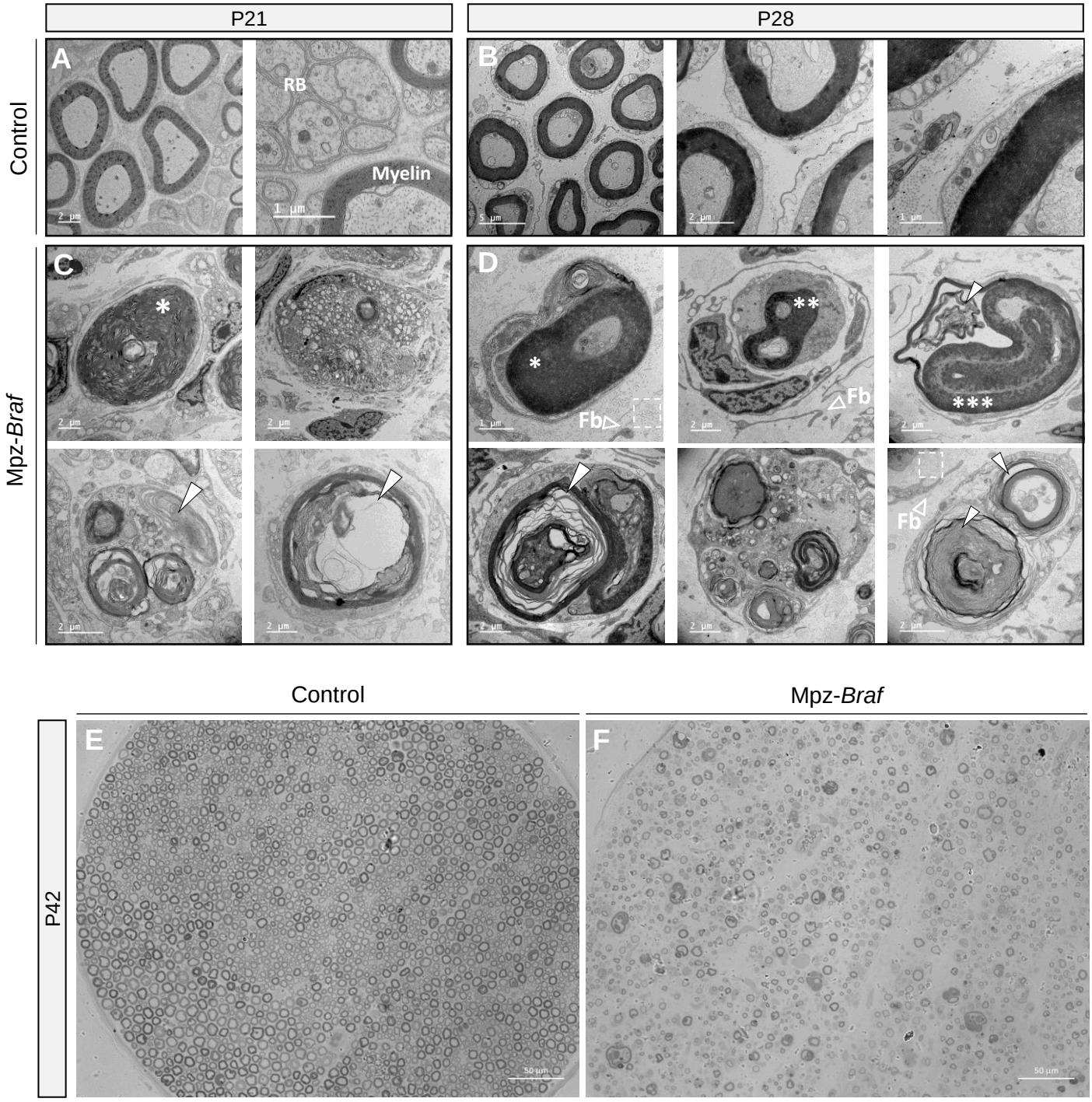
P21
P28
Control
Mpz-*Braf*
A
B
C
D
RB
Myelin
Fb
E
F
P42
Control
Mpz-*Braf*

Figure 5

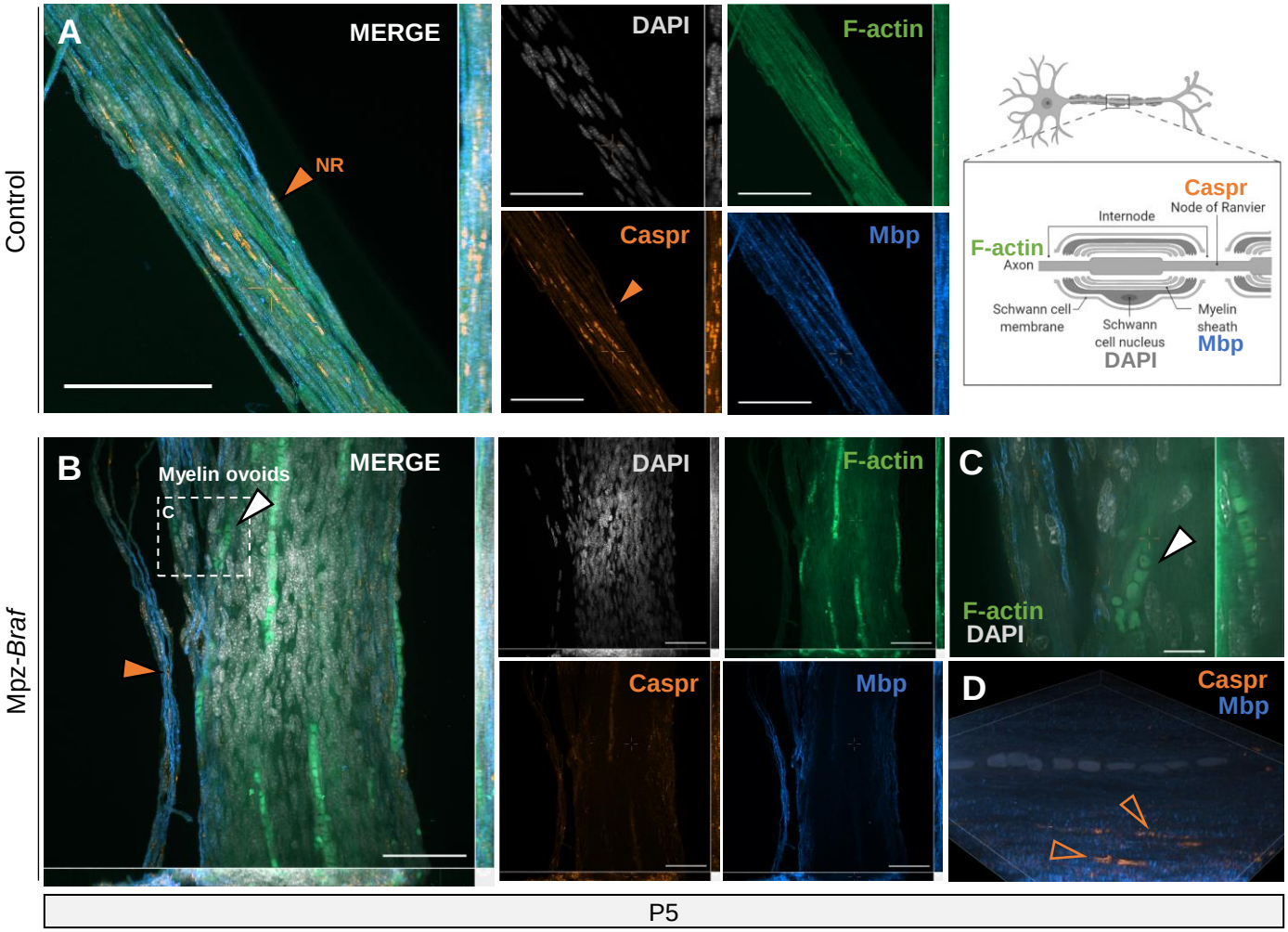
Control
A
MERGE
NR
DAPI
F-actin
Caspr
Mbp
Caspr
Node of Ranvier
Internode
F-actin
Axon
Schwann cell membrane
Schwann cell nucleus
DAPI
Myelin sheath
Mbp
Mpz-Braf
B
Myelin ovoids
C
MERGE
DAPI
F-actin
Caspr
Mbp
C
F-actin
DAPI
D
Caspr
Mbp
P5

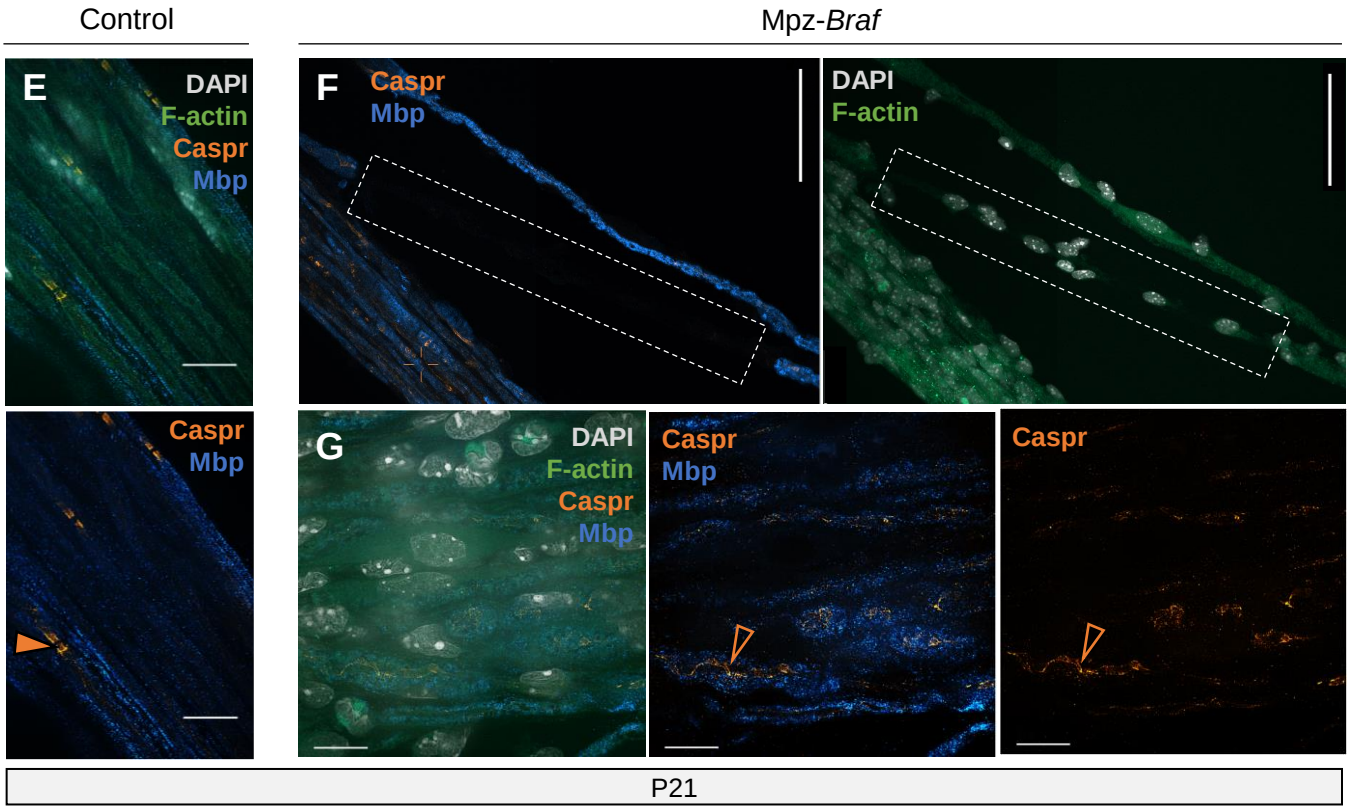
Control
Mpz-Braf
E
DAPI
F-actin
Caspr
Mbp
Caspr
Mbp
F
Caspr
Mbp
DAPI
F-actin
G
DAPI
F-actin
Caspr
Mbp
Caspr
Mbp
Caspr
P21

Figure 6

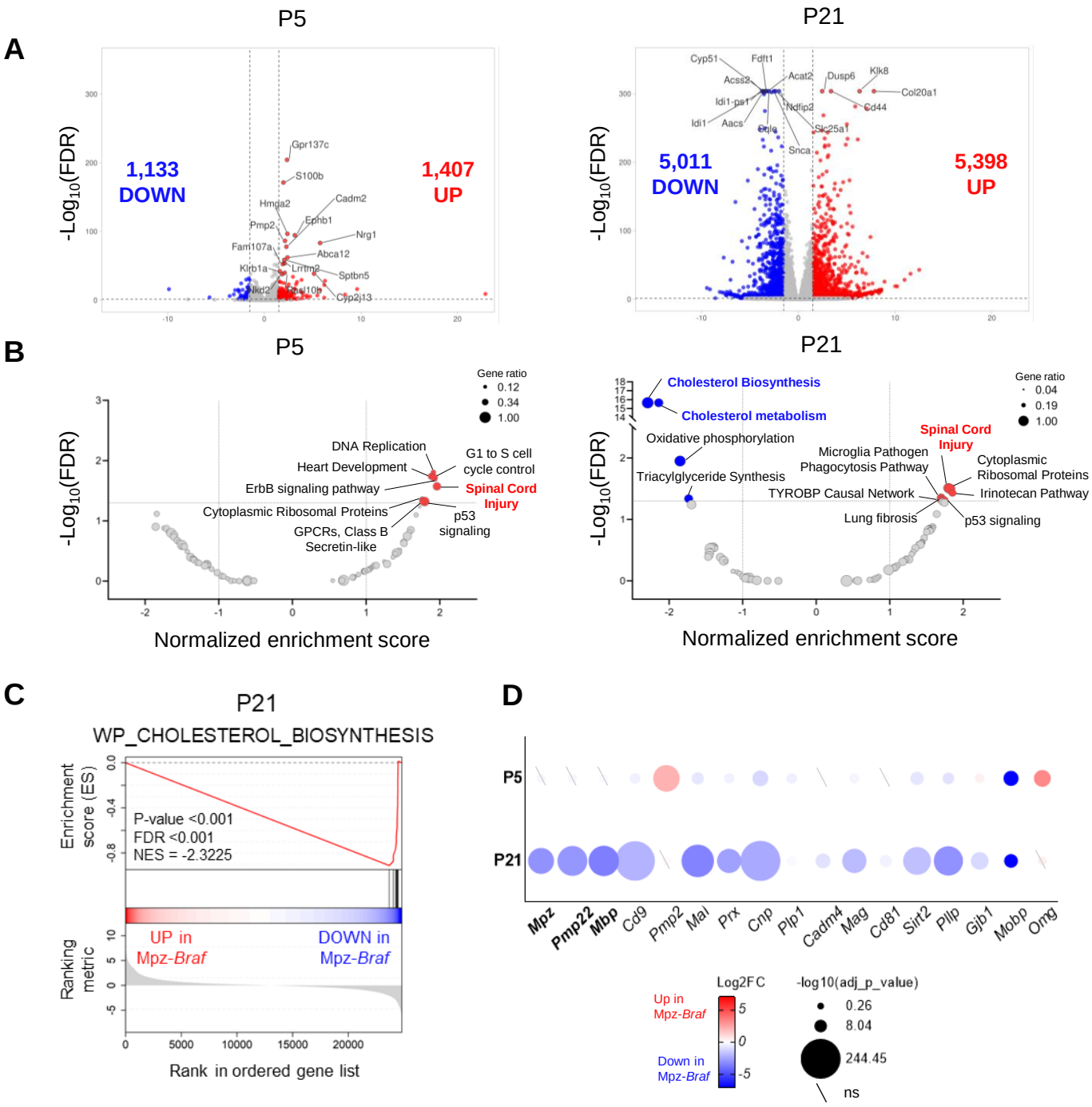
A
P5
P21
-Log10(FDR)
1,133
DOWN
1,407
UP
5,011
DOWN
5,398
UP
Gpr137c
S100b
Cadm2
Hmga2
Ephb1
Pmp2
Nrg1
Fam107a
Abca12
Klrb1a
Lrrtm2
Sptbn5
Nkd2
Cyp2j13
Cyp51
Fdft1
Acss2
Acat2
Dusp6
Klk8
Col20a1
Idi1-ps1
Ndfip2
Cd44
Idi1
Aacs
Slc25a1
Snca
B
P5
P21
Gene ratio
0.12
0.34
1.00
0.04
0.19
1.00
DNA Replication
Heart Development
G1 to S cell cycle control
ErbB signaling pathway
Spinal Cord Injury
Cytoplasmic Ribosomal Proteins
p53 signaling
GPCRs, Class B Secretin-like
Cholesterol Biosynthesis
Cholesterol metabolism
Oxidative phosphorylation
Triacylglyceride Synthesis
Microglia Pathogen Phagocytosis Pathway
TYROBP Causal Network
Cytoplasmic Ribosomal Proteins
Irinotecan Pathway
Lung fibrosis
p53 signaling
Normalized enrichment score
C
P21
WP_CHOLESTEROL_BIOSYNTHESIS
Enrichment score (ES)
P-value <0.001
FDR <0.001
NES = -2.3225
Ranking metric
UP in Mpz-Braf
DOWN in Mpz-Braf
Rank in ordered gene list
D
P5
P21
Mpz
Pmp22
Mbp
Cd9
Pmp2
Mal
Prx
Cnp
Plp1
Cadm4
Mag
Cd81
Sirt2
Pllp
Gjb1
Mobp
Omg
Log2FC
Up in Mpz-Braf
Down in Mpz-Braf
-log10(adj_p_value)
0.26
8.04
244.45
ns

Figure 7

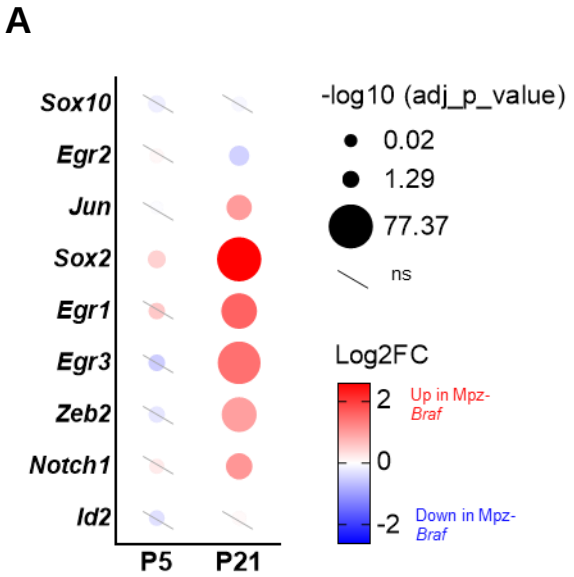

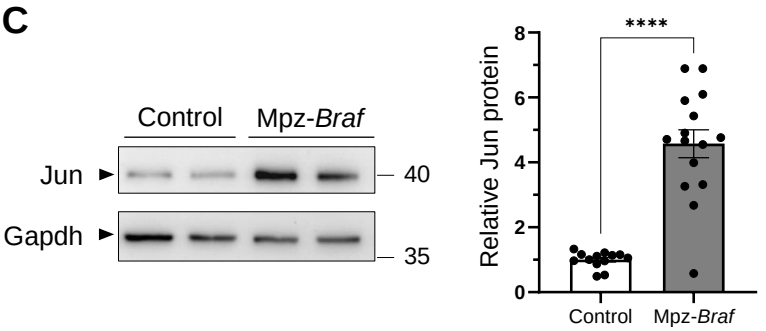

D

	Egr2-Cre$^{+/°}$ x *LSL- Braf*$^{V600E/+}$				
	WT$^{+/+}$	*Egr2*-Cre$^{+/°}$	*LSL-Braf*$^{V600E/+}$	*Egr2*-Cre; *Braf*$^{V600E/+}$	Total
Expected	20 (25%)	20 (25%)	20 (25%)	20 (25%)	80 (100%)
Observed	34 (42,5%)	21 (26,25%)	25 (31,25%)	**0 (0%)**	80 (100%)

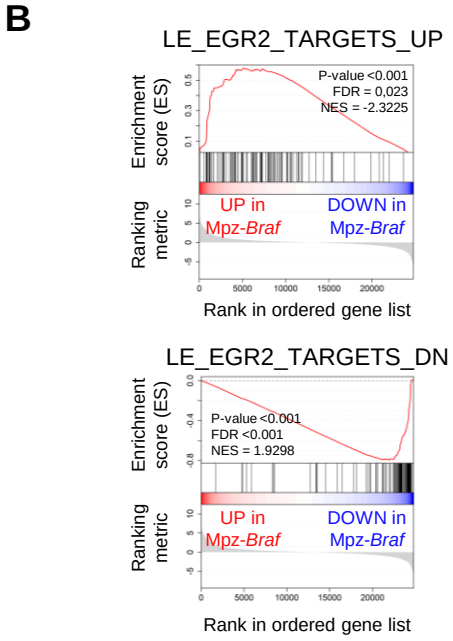

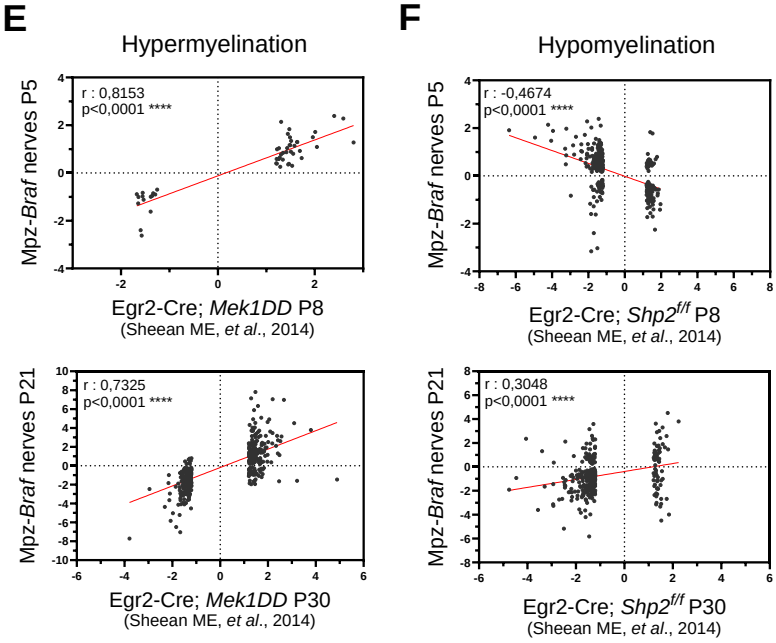

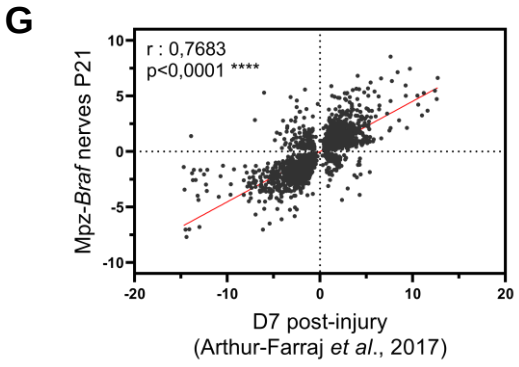

Figure 8

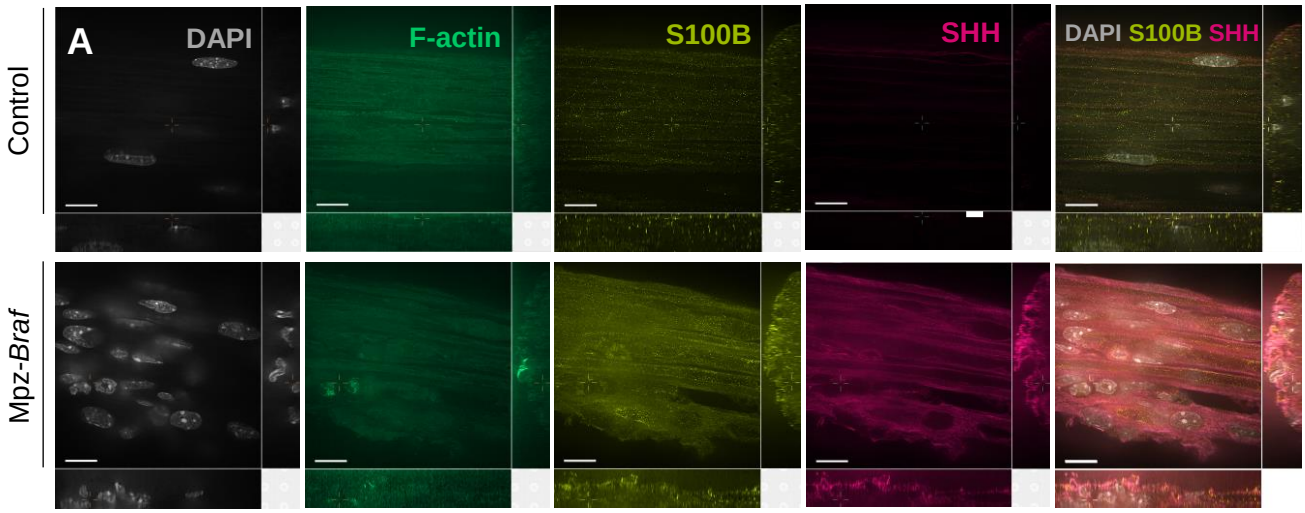
A
DAPI
F-actin
S100B
SHH
DAPI S100B SHH
Control
Mpz-Braf

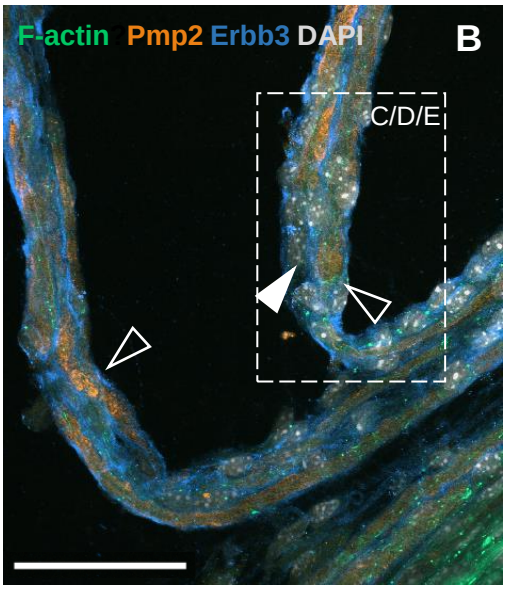
F-actin Pmp2 Erbb3 DAPI
B
C/D/E

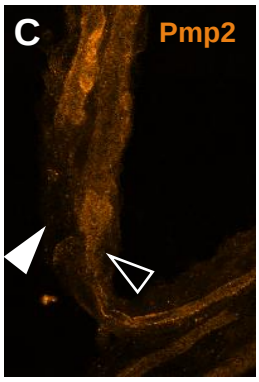
C
Pmp2

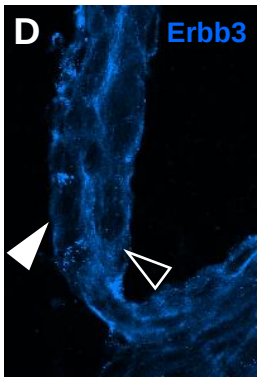
D
Erbb3

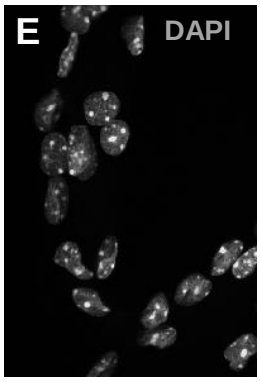
E
DAPI

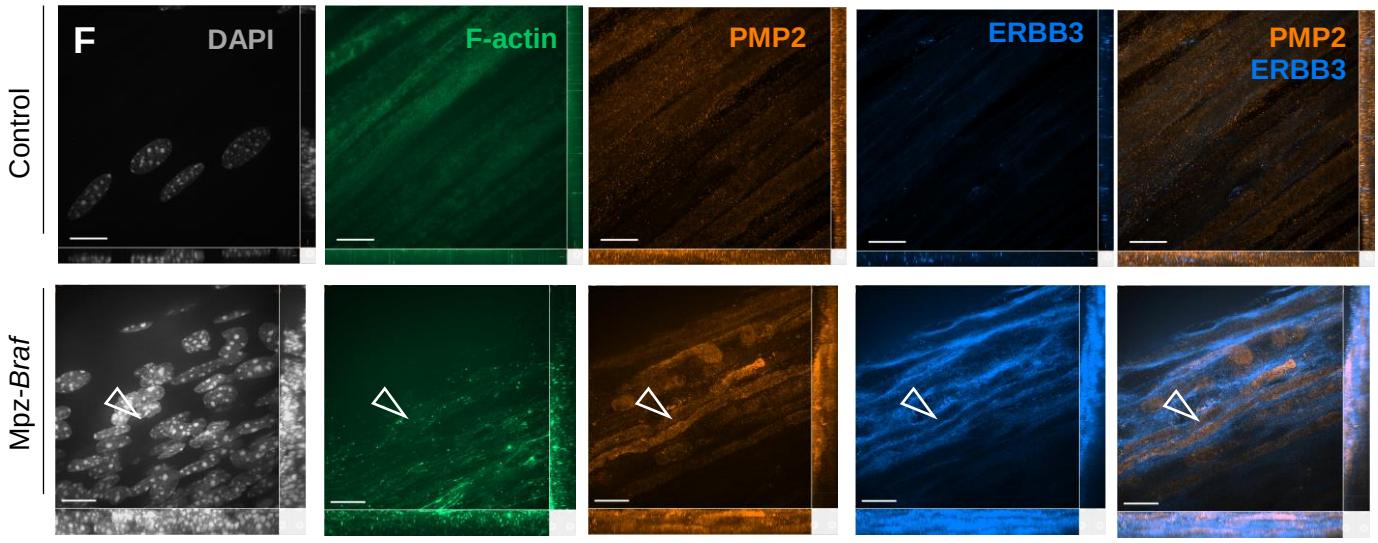
F
DAPI
F-actin
PMP2
ERBB3
PMP2
ERBB3
Control
Mpz-Braf

Figure 9

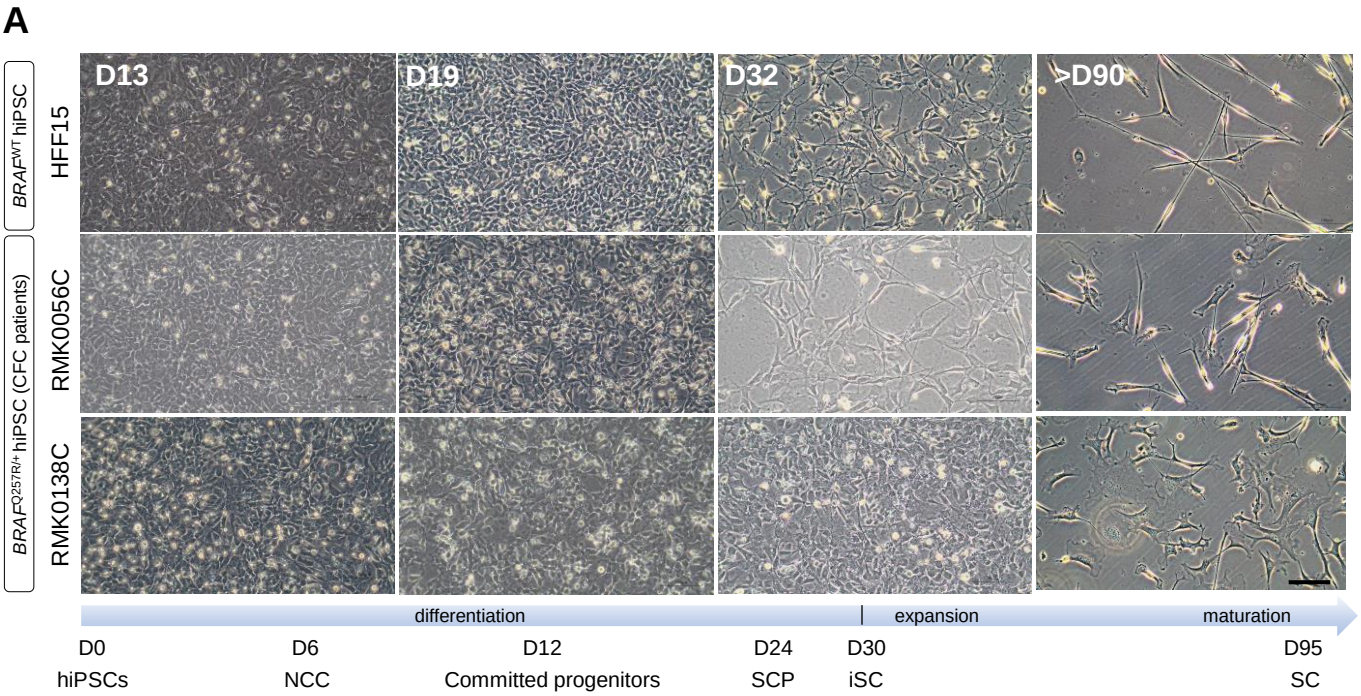
A
D13
D19
D32
>D90
BRAFWT hiPSC
HFF15
BRAFQ257R/+ hiPSC (CFC patients)
RMK0056C
RMK0138C
differentiation
expansion
maturation
D0
hiPSCs
D6
NCC
D12
Committed progenitors
D24
SCP
D30
iSC
D95
SC

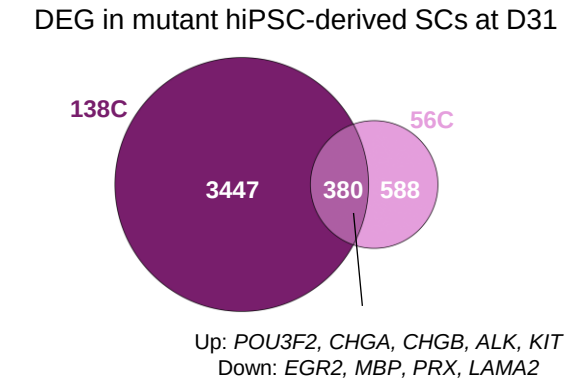
B
DEG in mutant hiPSC-derived SCs at D31
138C
56C
3447
380
588
Up: POU3F2, CHGA, CHGB, ALK, KIT
Down: EGR2, MBP, PRX, LAMA2

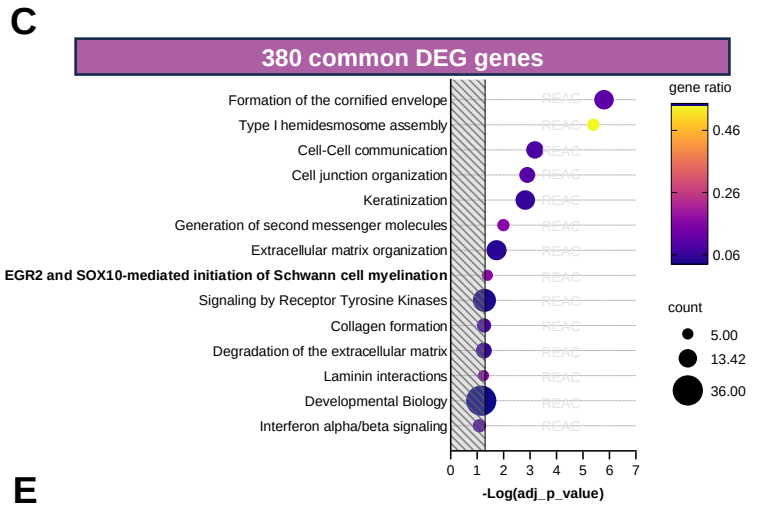
C
380 common DEG genes
Formation of the cornified envelope
Type I hemidesmosome assembly
Cell-Cell communication
Cell junction organization
Keratinization
Generation of second messenger molecules
Extracellular matrix organization
EGR2 and SOX10-mediated initiation of Schwann cell myelination
Signaling by Receptor Tyrosine Kinases
Collagen formation
Degradation of the extracellular matrix
Laminin interactions
Developmental Biology
Interferon alpha/beta signaling
REAC
gene ratio
0.46
0.26
0.06
count
5.00
13.42
36.00
0 1 2 3 4 5 6 7
-Log(adj_p_value)

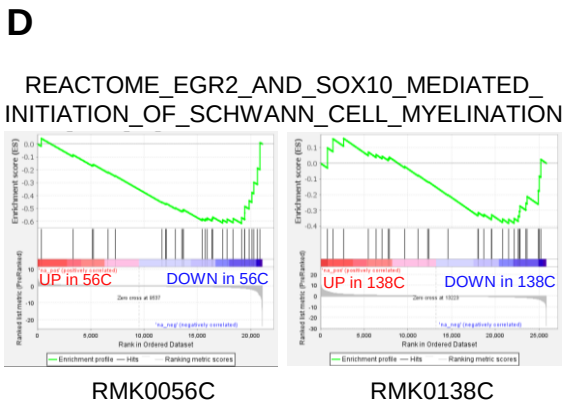
D
REACTOME_EGR2_AND_SOX10_MEDIATED_
INITIATION_OF_SCHWANN_CELL_MYELINATION
UP in 56C
DOWN in 56C
UP in 138C
DOWN in 138C
RMK0056C
RMK0138C

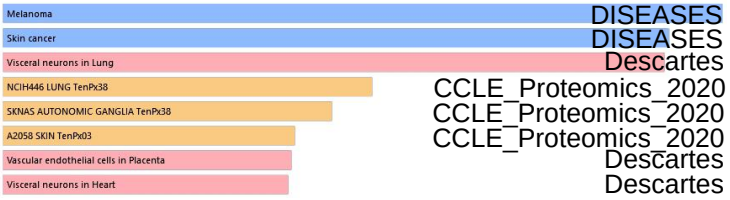
E
Melanoma
DISEASES
Skin cancer
DISEASES
Visceral neurons in Lung
Descartes
NCIH446 LUNG TenPx38
CCLE_Proteomics_2020
SKNAS AUTONOMIC GANGLIA TenPx38
CCLE_Proteomics_2020
A2058 SKIN TenPx03
CCLE_Proteomics_2020
Vascular endothelial cells in Placenta
Descartes
Visceral neurons in Heart
Descartes

Supplementary Figure 1

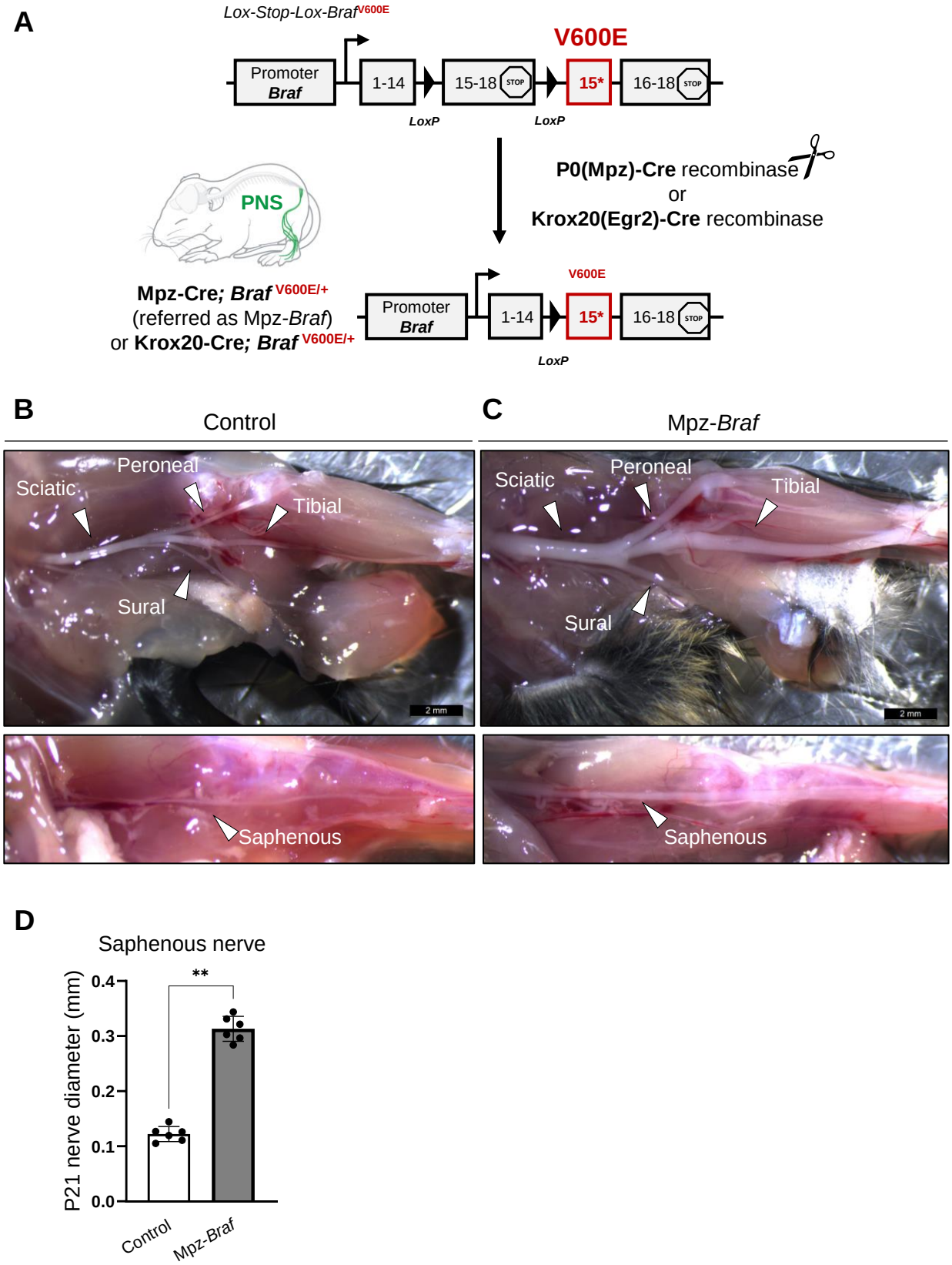

Supplementary Figure 2

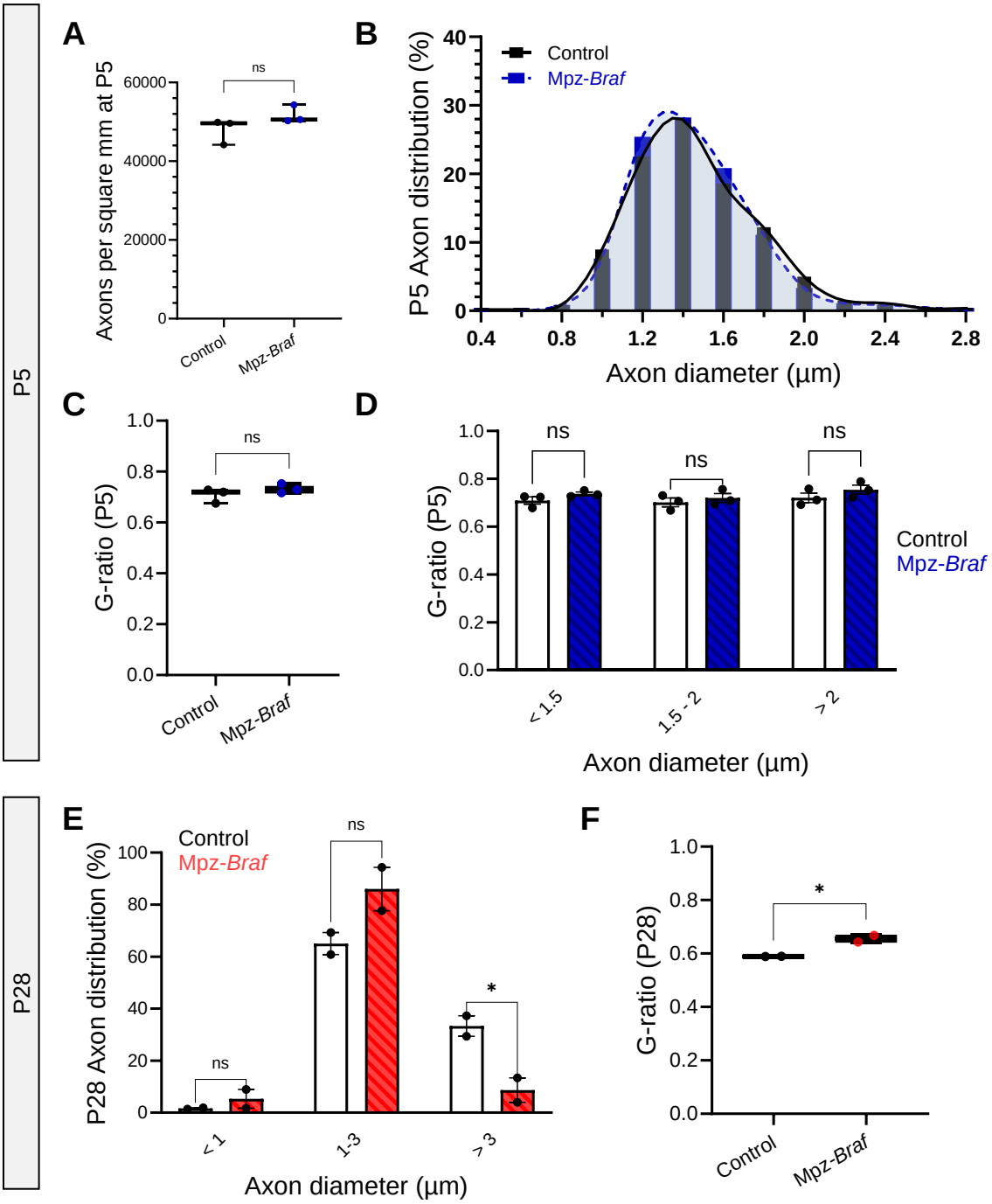

Supplementary Figure 3

A

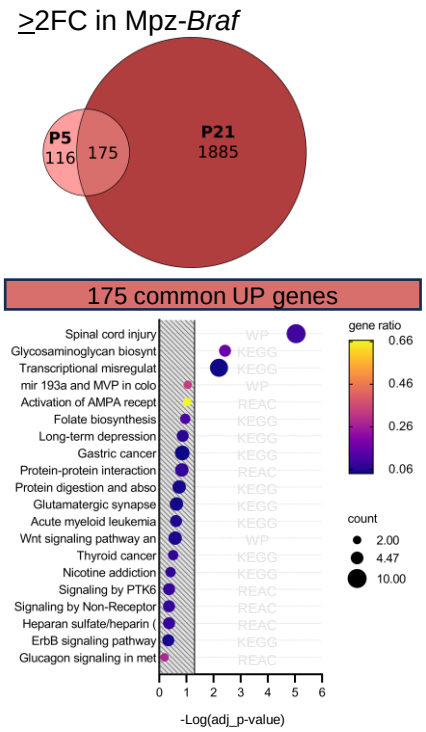

B

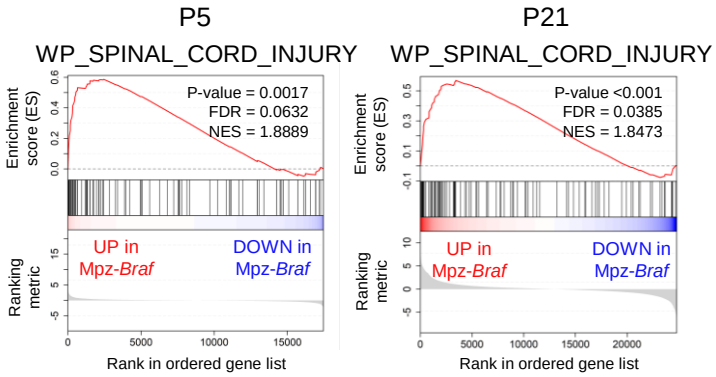

C

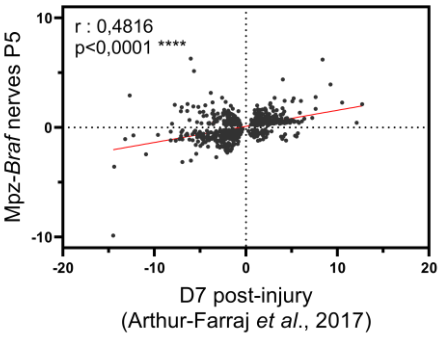

D
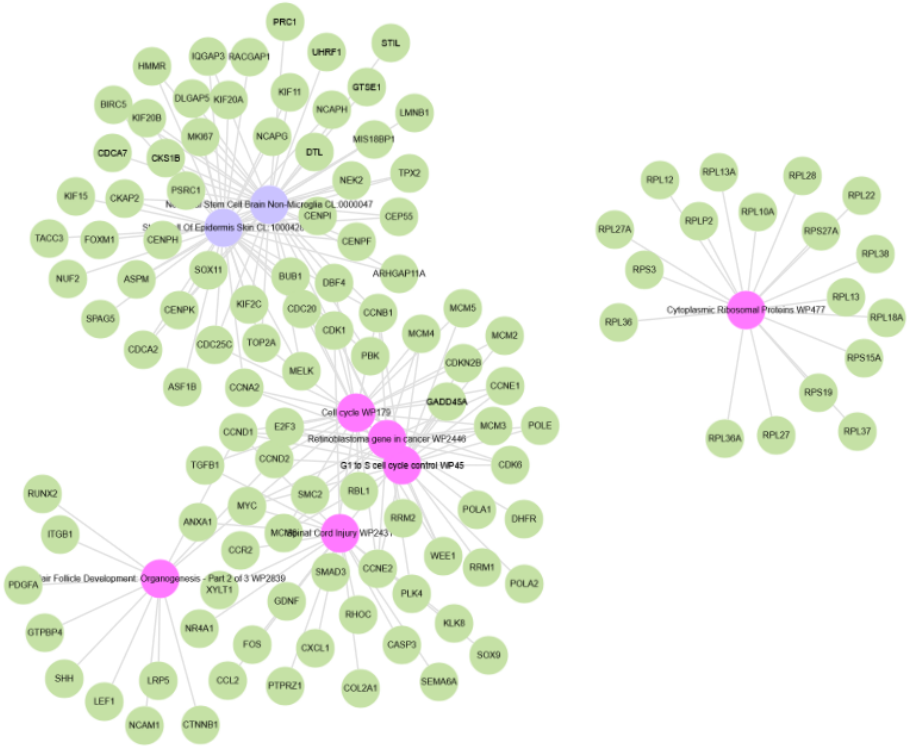
		p-value	q-value	z-score	combined score
Tabula_Muris	Stem Cell Of Epidermis Skin CL:1000428	2.3514e-32	2.422e-30	23.42	1705
Tabula_Muris	Neuronal Stem Cell Brain Non-Microglia CL:0000047	1.6779e-30	8.641e-29	21.25	1457
WikiPathway_2021_Human	G1 to S cell cycle control WP45	2.2345e-12	1.01e-9	10.65	285.8
WikiPathway_2021_Human	Cell cycle WP179	4.9693e-12	1.1231e-9	6.675	173.7
WikiPathway_2021_Human	Retinoblastoma gene in cancer WP2446	1.2897e-11	1.9432e-9	8.041	201.6
WikiPathway_2021_Human	Hair Follicle Development: Organogenesis - Part 2 of 3 WP2839	1.2344e-9	1.3949e-7	15.02	308.1
WikiPathway_2021_Human	Cytoplasmic Ribosomal Proteins WP477	7.9014e-9	7.1428e-7	6.38	119
WikiPathway_2021_Human	Spinal Cord Injury WP2431	2.8373e-8	0.0000021374	5.142	89.35